MICROCOPY RESOLUTION TEST CHART
NATIONAL BUREAU OF STANDARDS 1963

SECURITY CLASSIFICATION OF THIS PAGE *(When Data Entered)*

REPORT DOCUMENTATION PAGE	READ INSTRUCTIONS BEFORE COMPLETING FORM

1. REPORT NUMBER	2. GOVT ACCESSION NO.	3. RECIPIENT'S CATALOG NUMBER
AFIT/CI/NR 87-XXXT 111T		

4. TITLE *(and Subtitle)*	5. TYPE OF REPORT & PERIOD COVERED
The Effects of a Geomagnetic Storm on Thermospheric Circulation	THESIS/DISSERTATION
	6. PERFORMING ORG. REPORT NUMBER

7. AUTHOR(s)	8. CONTRACT OR GRANT NUMBER(s)
Douglas George Brinkman	

9. PERFORMING ORGANIZATION NAME AND ADDRESS	10. PROGRAM ELEMENT, PROJECT, TASK AREA & WORK UNIT NUMBERS
AFIT STUDENT AT: University of California	

11. CONTROLLING OFFICE NAME AND ADDRESS	12. REPORT DATE
AFIT/NR WPAFB OH 45433-6583	1987
	13. NUMBER OF PAGES
	109

14. MONITORING AGENCY NAME & ADDRESS(*if different from Controlling Office*)	15. SECURITY CLASS. *(of this report)*
	UNCLASSIFIED
	15a. DECLASSIFICATION DOWNGRADING SCHEDULE

16. DISTRIBUTION STATEMENT *(of this Report)*

APPROVED FOR PUBLIC RELEASE; DISTRIBUTION UNLIMITED

17. DISTRIBUTION STATEMENT *(of the abstract entered in Block 20, if different from Report)*

DTIC
ELECTE
NOV 1 6 1987
D

18. SUPPLEMENTARY NOTES

APPROVED FOR PUBLIC RELEASE: IAW AFR 190-1

LYNN E. WOLAVER 23 Sep 87
Dean for Research and
Professional Development
AFIT/NR

19. KEY WORDS *(Continue on reverse side if necessary and identify by block number)*

20. ABSTRACT *(Continue on reverse side if necessary and identify by block number)*

DD FORM 1473 EDITION OF 1 NOV 65 IS OBSOLETE
1 JAN 73

SECURITY CLASSIFICATION OF THIS PAGE *(When Data Entered)*

87 10 28 172

AD-A186 638
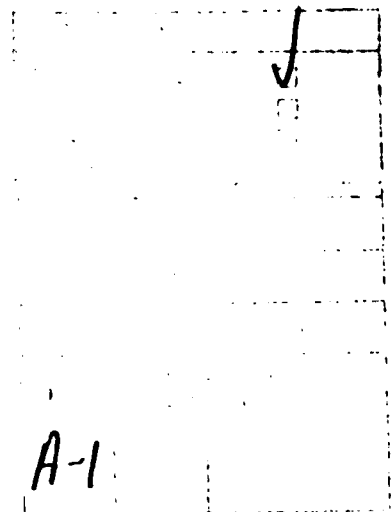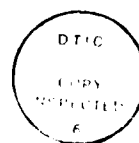
UNIVERSITY OF CALIFORNIA

Los Angeles

The Effects of a Geomagnetic

Storm on Thermospheric Circulation

A thesis submitted in partial satisfaction of the

requirements for the degree Master of Science
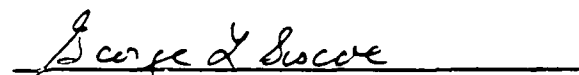
in Atmospheric Science

by

Douglas George Brinkman

1987

The thesis of Douglas George Brinkman is approved.

Robert L. McPherron

George L. Siscoe

S. V. Venkateswaran, Committee Chair

University of California, Los Angeles

1987

To my loving parents. George and Janeen Brinkman.

who taught me the value of education.

TABLE OF CONTENTS

LIST OF FIGURES

LIST OF TABLES

ACKNOWLEDGMENTS

co-authors listed in this publication directed and supervised the research which forms the basis for that part of the manuscript.

Finally, I wish to thank the United States Air Force for giving me the opportunity to do graduate work here at UCLA.

ABSTRACT OF THE THESIS

The Effects of a Geomagnetic

Storm on Thermospheric Circulation

by

Douglas George Brinkman

Master of Science in Atmospheric Science

University of California, Los Angeles, 1987

Professor S. V. Venkateswaran, Chair

The motions of the thermosphere and its interactions with the iono-
sphere during a geomagnetic storm are of current interest to space
scientists. A two-dimensional model was used to simulate the thermo-
spheric response to the impulsive high-latitude heating associated with
a geomagnetic storm. The storm-induced motions can be characterized by
an initial period of transient waves followed by the development of a
mean circulation. These motions generate an electrical current system
that is on the same order of magnitude as, and in the opposite sense
to the normal S_q current system. Model simulated winds and electrical
currents were then compared to observations.

I INTRODUCTION

The motions of the thermosphere and its interaction with the iono-
sphere during a geomagnetic storm are of current interest to space sci-
entists. The thermosphere is that part of the earth's atmosphere that
extends from 80 km to 450 km. It is composed mainly of neutral partic-
les with temperatures ranging from 180K at the mesopause to well over
1000K at its upper reaches. An integral part of the thermosphere is
the ionosphere which is composed of several layers of ionized partic-
les that reside within the thermosphere. The response of the thermo-
sphere to various inputs and the subsequent interaction of neutrals
and ionized particles can yield interesting results.

Of particular interest is how these interactions influence long
range radio communications and satellite drag. The feasiblity and
quality of radio communications is dependent on the state of the iono-
sphere and hence the motions of the thermosphere. An increase in drag
can greatly affect the orbit of low-to-medium altitude satellites. A
vivid example of this was the orbit decay and reentry of Skylab.

The purpose of this study was to aquaint myself with the two di-
mensional thermospheric model of Richmond and Matsushita (1975), to
simulate the hydrodynamical and electrodynamical responses to a gene-
ric geomagnetic storm , and to simulate the responses for two actual
geomagnetic storms to see how well the model reproduced the time de-
pendent storm-time features of the thermosphere. Chapter two describes
the quiet and disturbed thermosphere including basic structure, energy
sources, observation methods, and observations of the quiet-time and

1

storm-time neutral wind circulation. Chapter three describes the two-dimensional time dependent thermospheric model of Richmond and Matsushita (1975) used in this study. Basic characteristics of the model and mode inputs are discussed. Chapter four discusses the model outputs as they apply to a generic geomagnetic storm. Chapter five describes some of the electrodynamic aspects of the thermosphere and how it is affected by the storm-time circulation. Chapter six compares two geomagnetic storms analyzed by Mazaudier et al. (1985) with model outputs. Finally, chapter seven provides conclusions and discusses plans for future studies of thermospheric processes.

II BASIC PROPERTIES OF THE QUIET AND DISTURBED THERMOSPHERE

The structure of the thermosphere is the result of a complex inter-action between solar energy inputs, composition, and circulation. It is difficult to describe any one part of this system without referring to the effects of the other parts. Several excellent reviews of the thermosphere-ionosphere system, have been written by Hanson and Carlson (1977), Killeen (1987), Richmond (1983), Rishbeth (1972), and Roble (1977).

This section briefly summarizes that material and is not meant to be an all inclusive discussion of the thermosphere-ionosphere system. The effects of solar radiation inputs on composition and temperature are described. Energy inputs from the solar wind are discussed. This is followed by a description of the resulting circulation from both these energy inputs. To round out the discussion, observational tech-niques are described and a summary of neutral wind observations for both quiet and storm-times are presented.

Energy from the sun can be divided into two distinct forms, that which is associated with electromagnetic radiation and that which is associated with the solar wind. Most of the sun's electromagnetic radiation is in the visible part of the spectrum and passes through the thermosphere to the ground and lower atmosphere where it is absorbed or reflected back to space. Solar electromagnetic radiation with wave-lengths less then 200nm is absorbed by constituents in the thermosphere such as O, O_2, N_2 , and NO.

Composition

Below 80 km. the composition of the the atmosphere is 78% N_2. 21% O_2. and 1% of the other constituents such as O_3, CO_2, and H_2O. Neutral gas composition above 80 km is dependent on solar extreme ultraviolet (EUV) radiation and ultraviolet (UV) radiation with wavelengths less than 200nm which photodissociates molecules into their atomic form. The reaction:

$$O_2 + h\nu = O + O$$
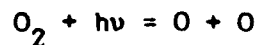
is very efficient and is the dominate reaction at these levels. Recombination of oxygen atoms back to an oxygen molecule requires a third body such that:

$$O + O + M = O_2 + M.$$
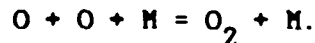
This reaction is very slow above 90 km. Oxygen atoms must therefore, be transported downward in order to recombine. This leads to oxygen atoms being the major constituent of the thermosphere at 150 km.

Contributing to this maximum of atomic oxygen is the turbopause, which is at roughly 110 km. Above this level molecular diffusion becomes important. As a result constituents become segregated in altitude according to molecular weight. Heavier species maximize at lower thermospheric altitudes while lighter species such as O become dominant at higher altitudes. Diffusive equilibrium is dependent on tempera-

4

ture, and strong diurnal variation of temperature causes the composit-
ional structure of the thermosphere to exhibit a corresponding strong
diurnal variation.

Temperature

Between 150 and 300 km. neutral heating through the absorption of
solar EUV by oxygen atoms dominates. Above 300 km, EUV absorption is
still important but the effects of magnetospheric processes also
matter. Below 150 km, O_2 absorption of solar UV in the Schumann-Runge
continuwun (130-175nm) dominates, and below 100 km O_2 absorption in the
Schumann-Runge bands (175-200nm) is important. Below 80 km, O_3 becomes
the dominant absorber.

As described above, there are a wide variety of absorbers in the
thermosphere. However, above 90 km there are few effective radiators
of thermal energy. During solar minimum, The global mean vertical
temperature structure is determined by a balance between local heating,
and molecular and eddy thermal conduction downward to the mesopause at
80 km where CO_2 and O_3 can radiate this energy back to space. The re-
sultant temperature ranges from 180-200K at 80 km to a temperature
that reaches to 1500K and above at 300 km. Molecular conduction at the
upper levels is so fast that large vertical temperature gradients can-
not form and the thermosphere becomes isothermal. The temperature at
this level is know as the exospheric temperature. (The exosphere being
that part of the atmosphere where collisions are so rare, that partic-
les move in ballistic orbits constrained only by gravity.)

The level of solar activity also plays a role in determining temperature structure. It is associated with two time scales. One time scale is the 27 day solar rotation period and the other is the 11 year sunspot cycle. Active regions such as sunspots, plages, and coronal condensations, which are visible on the solar disk, rotate with the sun. They are more prevalent at maximums in the 11 year solar cycle and are indicative of enhanced solar output. This enhancement causes the solar EUV radiation to double from solar minimum to solar maximum, resulting in a 700K change in the mean exospheric temperature from minimum to maximum. Also during solar max, radiative cooling due to NO can play a significant role in determining thermospheric temperature. In addition, the exospheric temperature varies greatly from day to day. Figure 1. shows exospheric temperatures for different levels of geomagnetic activity.

Temperature maximizes at the subsolar point (with a slight lag due to conduction effects) and minimizes at the antisolar point. On a seasonal basis, the temperature maximum follows the subsolar point through its yearly cycle. Maximum temperatures are observed at the equinoxes and minima at solstices. The diurnal temperature variation is on the order of 20-30% of the mean exospheric temperature. This large diurnal variation demonstrates the high degree of control that solar electromagnetic radiation exercises in determining thermospheric temperature.
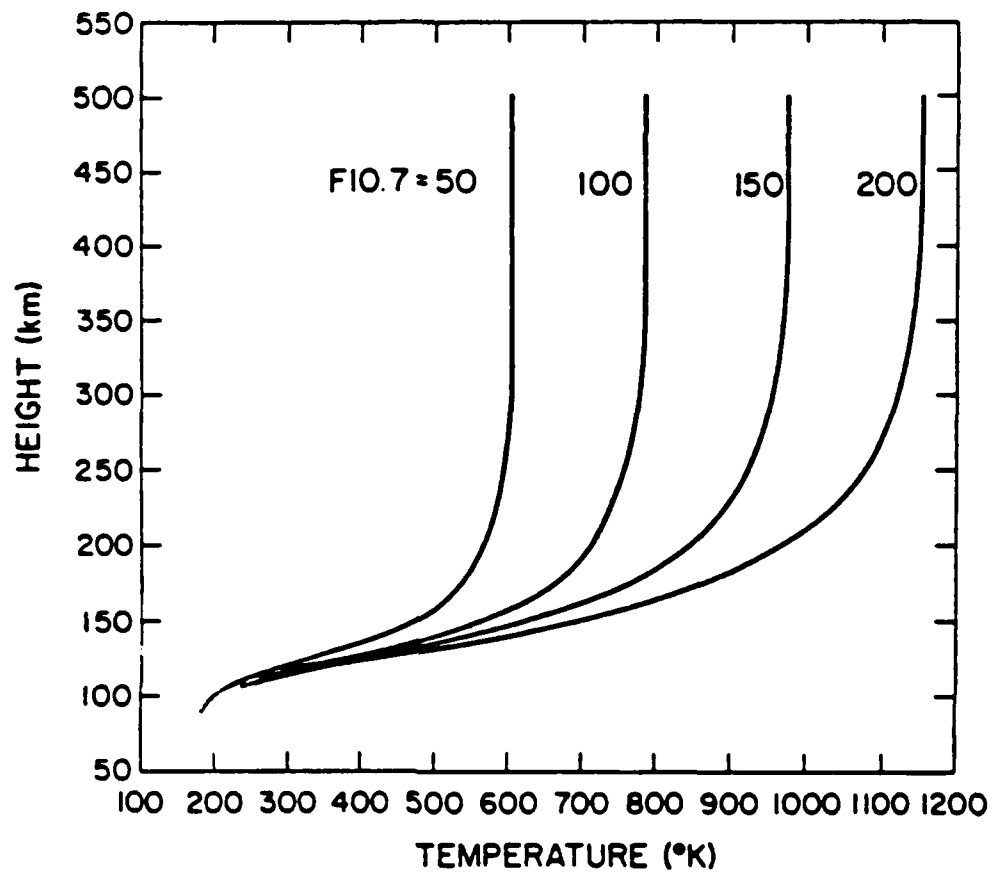
Figure 1. Global mean thermospheric temperature profiles for various
levels of solar activity. The F10.7cm radio flux is an indicator of
the solar EUV output (from Roble, 1977).

Ionosphere

The earth is surrounded by a layer of ionized gas called the ionosphere which resides within the thermosphere. The ionosphere can be divided into two distinct parts: a low latitude ionosphere dominated by solar radiation (which is discussed here) and a polar ionosphere dominated by energetic particle precipitation and magnetospheric processes (which is discussed in the following section).

Several distinct layers of charged particles exist. The D region extends from 60-90 km (ion density of 10^2-10^4cm^{-3} during the day). The E region, which extends from 90-140 km (10^5cm^{-3}), is the result of the absorption of soft solar X-rays. The F region, which is divided into the F1 layer from 140-200 km and the F2 layer from 200 km to its peak at 300 km (10^6cm^{-3}), is the result of the absorption of solar EUV radiation from 20-90nm. Molecular ions dominate in the E and F1 regions, while O^+ is the dominate species in the F2 region.

Chapman (1931) first purposed that the ionization peaks were the result of the balance between solar photoionization and recombination. This explains the E and F1 region peaks but not the F2 region peak. It is downward ion diffusion that effectively puts a lid on the F2 layer and forms the peak.

There is also considerable variation in ionospheric density. Irregularities exist at all latitudes but predominately at high latitudes and at the equator. Ion density can vary on the order of 10^2 to 10^3cm^{-3} within a few kilometers.

Auroral Processes

The aurora is a sign that large amounts of energy are being deposited in the thermosphere, especially at high latitudes. Heating due to auroral processes can have a great influence on the basic state of the thermosphere and its circulation. During quiet times, the high latitude heating rate is about 1/10 of the solar heating rate ($5X10^{10}$ watts compared to $4X10^{11}$ watts at 120 km).

Energy from the solar wind is transferred to the neutral atmosphere through energetic particle precipitation, frictional dissipation of ionospheric currents, and ion drag forces, all of which result from the interaction of the solar wind with the earth's magnetic field.

Particle precipitation, as evidenced by the aurora, is the result of 10-0.5 Kev electrons traveling along field lines and colliding with oxygen atoms in the thermosphere. This leads to the following reaction:

$$O + e = O^+ + 2e \qquad \text{(ionization)}$$

The more energetic the electrons the deeper down into the atmosphere their energy is deposited. The resulting ionization provides a horseshoe shaped region of high electrical conductivity known as the auroral oval.

Solar wind interaction with the earth's magnetic field can drive currents along magnetic field lines. Discontinuites in the magnetospheric convection electric field ($\vec{V} \cdot \vec{E} \neq 0$) can lead to field-aligned

potential differences that generate field-aligned currents (Lyons, 1980). The field-aligned currents close through the auroral oval, where the frictional dissipation of these currents results in Joule heating.

Solar wind interaction with the magnetosphere also results in the generation of an electric field perpendicular to the magnetic field. High conductivity along field lines allows the electric field to be mapped down to the ionosphere. This provides a momentum source that sets the ions and the electrons into motion. Electric fields at high latitudes range between 10 and 100 mV/m, which can impart electron drifts on the order of 200 to 2000 m/s. The higher values are seen during intense geomagnetic activity.

The ions collide with neutrals and drag the neutrals along their drift paths (ion drag). This is an important source of momentum at high latitudes. The collisions between ions and neutrals also provide heating and act as mechanical resistance to neutral wind motion. Hence, ion drag provides both a heat source and a momentum source to the thermosphere, although the effects tend to be confined to the high latitude region.

A geomagnetic storm can greatly enhance high latitude heating to a level equal to or exceeding heating from solar EUV and UV. By a geo-magnetic storm, what is meant is a disturbance in the solar wind that increases interaction with the earth's magnetic field. It results in the development of large electric fields and intense electrical cur-rents enhancing high latitude heating. A geomagnetic storm can last from several hours to several days and show up as a disturbance in

ground-based magnetic measurements. The source of the solar wind disturbance could be a solar flare, a coronal hole, or solar mass ejection. By enhancing the auroral processes already discussed, a geomagnetic storm can cause large variations in compostion, temperature, and circulation. These effects lag the storm by several hours and the lag time is longer the further one is away from the auroral zone. The amplitude of these changes depends on the magnitude of the storm. Energy deposited in the auroral zone is transferred to the rest of the globe via dynamic processes, and results in a global increase in exospheric temperature.

Circulation

One of the earliest ways of getting a handle on thermospheric circulation was through the use of semi-empirical models. The influence of atmospheric drag on earth orbiting satellites is a useful tool to study the thermosphere. Drag is related to atmospheric density. Jacchia (1965) used orbital changes of satellites due to drag effects to deduce a global distribution of neutral gas density above 120 km. This density distribution was then used to determine an exospheric temperature pattern which can be used as an input to a semi-empirical model such as developed by Dickinson et al. (1975), Hedin et al. (1977), and Hedin (1983). (Hedin (1983) is an updated version of Hedin et al.) These models use the temperature pattern and composition to derive a pressure field that in turn drives a wind field.

During quiet times, when solar EUV and UV are the dominant heat

11

sources, winds blow from the subsolar point to the antisolar point. This circulation exhibits generally upward motion on the dayside and downward motion on the nightside, with meridional winds blowing from the equator toward the pole, and zonal winds blowing eastward in the afternoon and westward in the morning. (See figure 2., which is from Roble, 1977; but was originally from Dickinson and Geisler, 1968.) On a seasonal basis the flow is from the equator to the poles at equinox and from the summer hemisphere to the winter hemisphere at solstice.

There can be large departures from the mean flow at high latitudes, where auroral heating is large compared to solar heating. Adding a heat source at high latitudes sets up a reverse circulation that counters the quiet-time winds. Additionally, variation in the heating source during a geomagnetic storm can generate gravity waves. At equinox, the circulation due to high latitude heating drives an average flow from high latitudes to low latitudes in both hemispheres as shown in figure 3., which is a schematic diagram from Roble (1977), based on computer simulations from Dickinson et al. (1975). Its magnitude depends on the level of geomagnetic activity. At solstice, increased geomagnetic activity enhances the flow in the summer hemisphere and reverses the flow in the winter hemisphere as shown in figure 4.(same source as figure 3.). On a day-to-day basis, however, the flow is highly variable.

Superimposed on these motions are the effects of upward propagating planetary waves, gravity waves, and tides. Tidal oscillations in particular can play a role in lower thermospheric motions. These oscillations are excited by the strong diurnal variation of EUV and UV

12
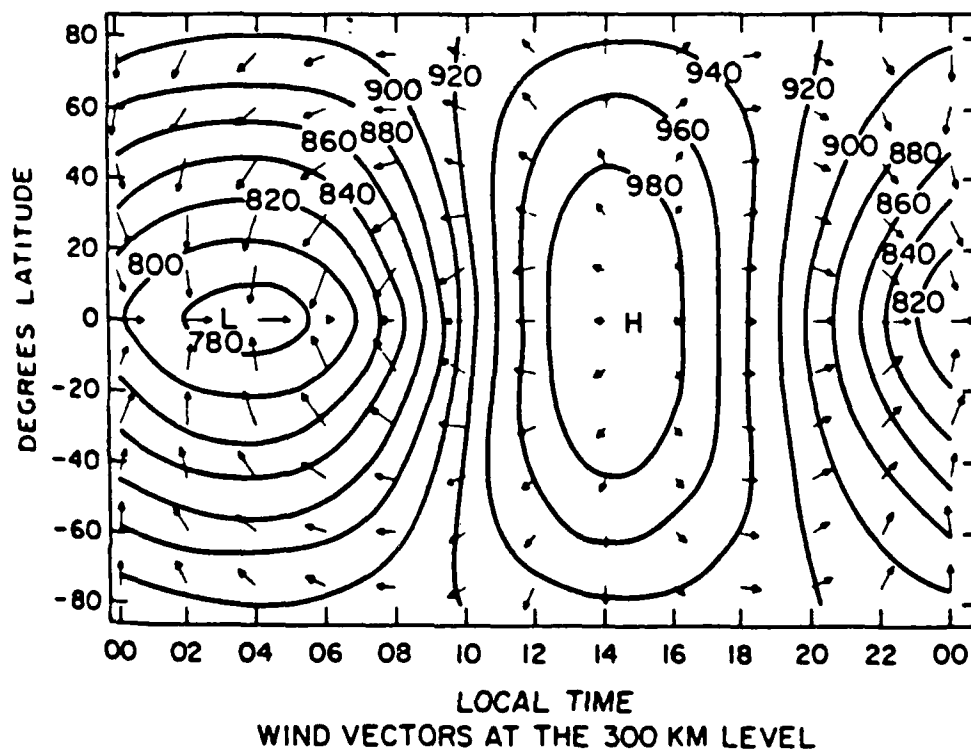
Figure 2. The global distribution of neutral gas temperatures at 300 Km based on an empirical model. The arrows show the wind pattern determined at 300 Km. The longest arrow represents a wind speed of 225 m/s (from Dickinson and Geisler, 1968; and Roble, 1977).

13
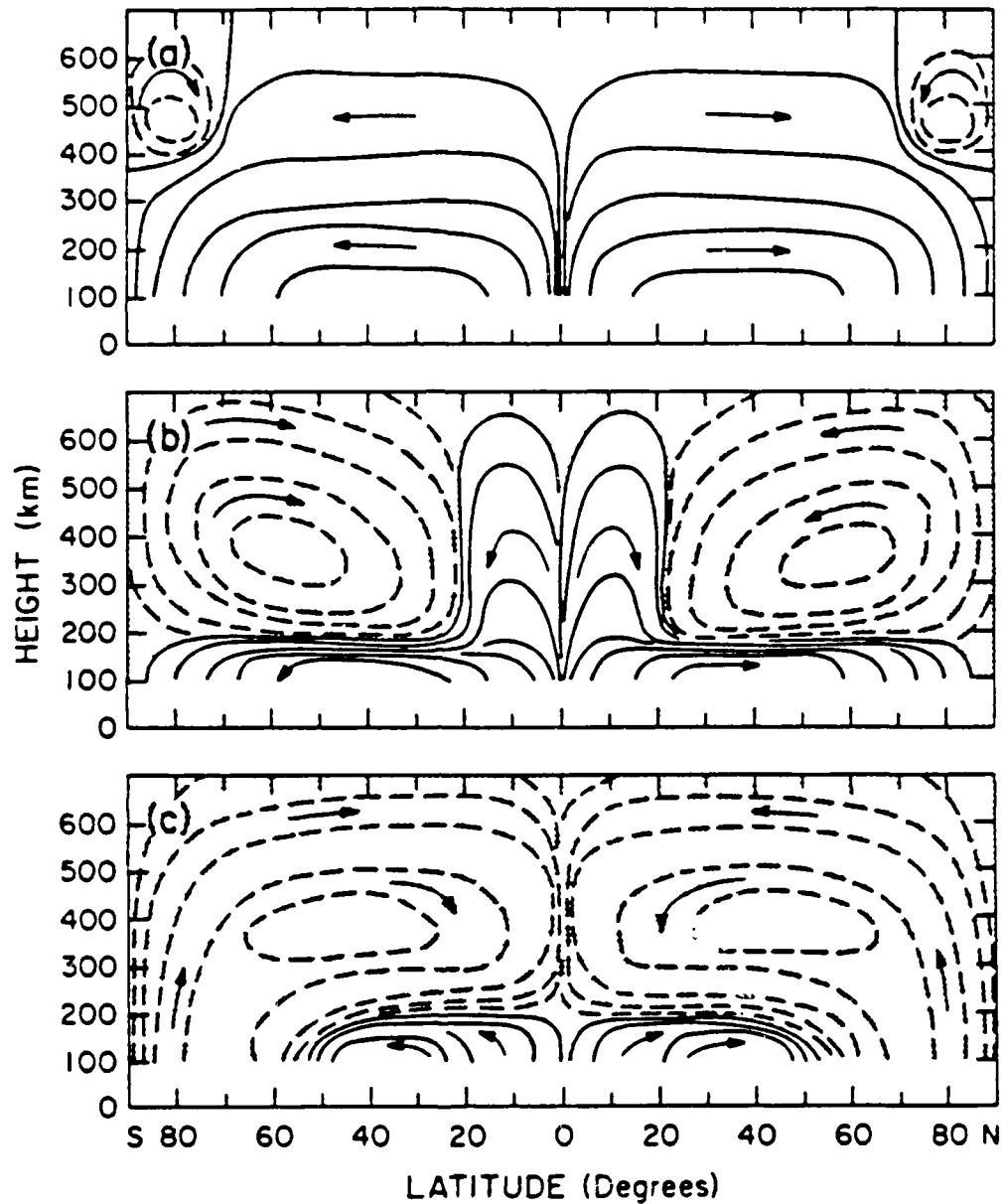
EQUINOX

Figure 3. Schematic diagram of the mean meridional circulation in the earth's thermosphere during equinox for various levels of auroral activity, (a) extremely quiet geomagnetic activity, (b) moderate activity (10^{11}W), and (c) intense geomagnetic activity (10^{12}). The contours schematically illustrate the mass flow, and the arrows indicate the direction of the motion (from Roble, 1977).
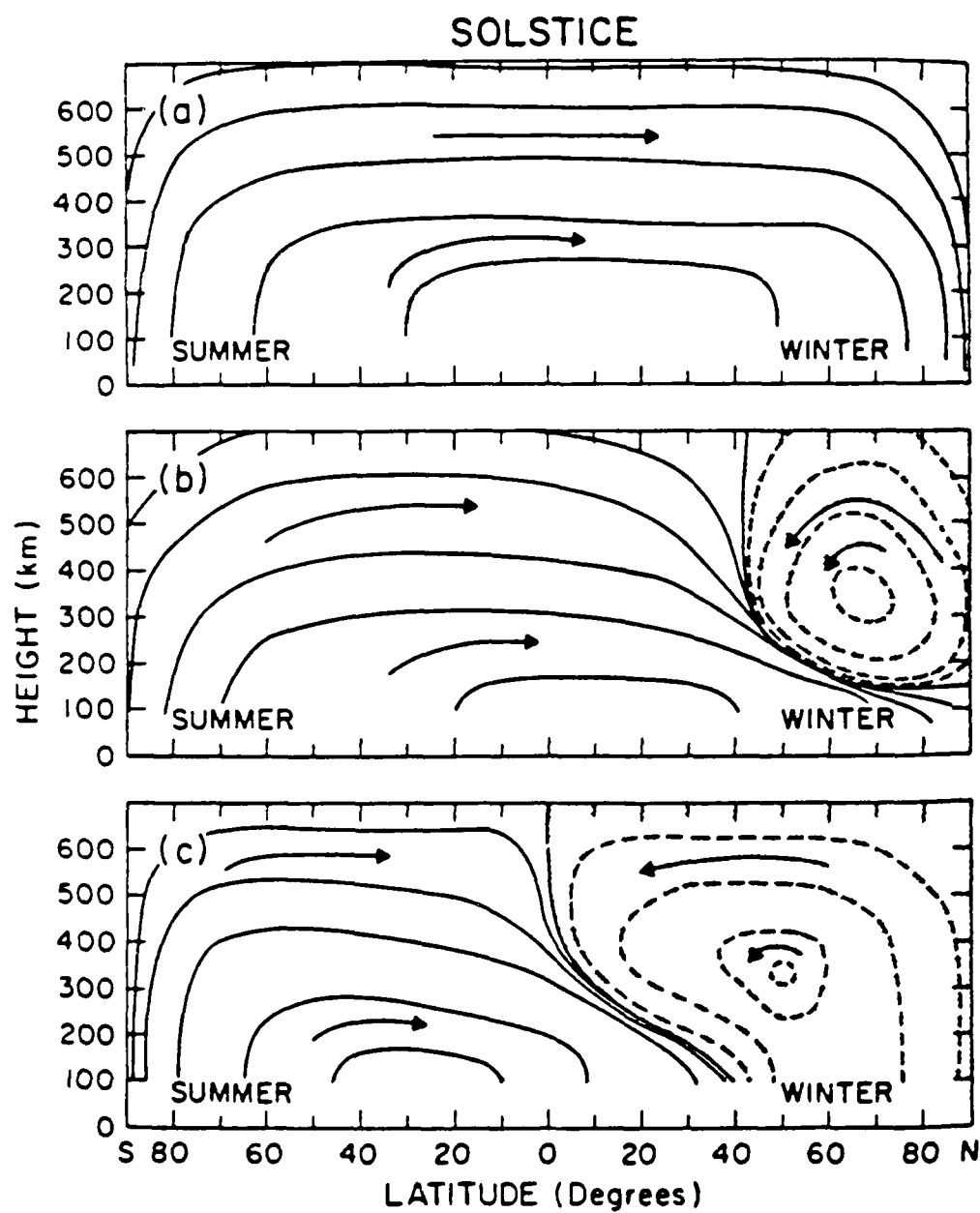
SOLSTICE

Figure 4.   Same as Figure 3. but at solstice (also from Roble, 1977).

absorption in the thermosphere and the absorption of UV by ozone and H_2O in the mesosphere and stratosphere. Some tidal modes remain trapped and don't propagate far from their generation place. Other modes propagate upwards and impart their energy to the lower thermosphere. The diurnal and semi-diurnal motions induced by these tides can generate electrical currents in the ionosphere.

Other forces that affect thermospheric circulation include viscous forces and ion drag forces. Kinematic molecular viscosity increases exponentially with height, and above 300 km motions are characterized by bulk motion.

Ion drag also affects air motions. On the dayside, ion density maximizes and results in collisions decreasing the wind speed. It also causes cross-isobaric flow from high to low pressure areas. At night when ion density is lower the effects of ion drag are lower and wind speeds are higher. Quiet-time circulation is hence a balance between pressure gradient, coriolis, and ion drag forces.

Observation Techniques

Observations of the thermosphere are made in several ways. The earliest measurements of neutral winds were made by radar observations of meteor trails at 80-100 km. This showed the influence of planetary waves, atmospheric tides, and gravity waves in the lower thermosphere and upper mesosphere. A second method was by observing the drifts of chemical releases from rockets. These drifts could then be used to deduce mean zonal and meridional winds. As mentioned earlier, the

16

effects of drag on low and medium orbiting satellites have been used to deduce exospheric temperature, and hence thermospheric winds. More recently, satellites in the Atmospheric Explorer series and the DE satellites, carrying spectrometers, have made measurements of ionospheric and thermospheric properties.

Ground-based measurements can be made by incoherent scatter radars (ISR) and Fabry-Perot interferometers (FPI). Incoherent scatter radars measure the energy backscattered from plasma density irregularities due to Thomson scattering. The doppler shift associated with this returned energy provides a direct measure of ion drifts. The magnitude and shape of the returned energy spectra provides ion density and plasma temperature. These data are then used to infer meridional neutral winds. Most of the ISR facilities are monostatic (one antenna) and are restricted to measuring only one component of ion velocity. At Millstone Hill, MA, for example, vertical ion drifts are measured. By subtracting out effects of ambipolar diffusion and electric fields (which are estimated), the meridional component of the neutral wind is inferred.

The French quadristatic incoherent scatter radar facility at St. Santin, France, and more recently the EISCAT ISR in Scandinavia are unique in that they are multistatic radars (multiple antennas) and can give the total ion velocity vector for the E and F regions. Below 110 Km, the neutral wind velocity is approximately equal to the ion velocity. Between, 110 km and 180 km, the ion velocity parallel to the magnetic field $(V_{1\parallel})$ is equal to the parallel component of the neutral wind $(V_{1\parallel})$. Multiplying $V_{1\parallel}$ by a geometrical factor, which is depend-

17

ent on station location, the meridional velocity is obtained. Above 180 km the effects of diffusion must be considered in calculating $V_{i\|}$. The electric field can also be determined. In the F region:

$$\vec{V}_{i\perp} = (\vec{E}_\perp \times \vec{B})/B^2 \ .$$

Thus by measuring $\vec{V}_{i\perp}$ (the ion velocity perpendicular to the magnetic field line), the electric field can be determined. High conductivity along magnetic field lines allows the F region electric field to be mapped down to the E region.

The use of incoherent scatter radars is limited to daytime in the E region, when ion densities are high, but at night F region measurements can still be made. Also at night, ground-based measurements can be made using a Fabry-Perot interferometer (FPI). Neutral winds are obtained by measuring the doppler shift of the 630nm red line emissions of O('D) at 250 km (the airglow level). By looking at the broadening of the doppler spectrum, temperature is obtained. FPIs are able to make measurements in both the meridional and zonal directions. The majority of neutral wind measurements have been made by this technique.

Observed Quiet-Time Neutral Winds and Temperatures

The majority of quiet-time neutral wind observations (summarized in Table 1.) have been made at mid-latitudes. Salah and Holt (1974) using the incoherent scatter radar at Millstone Hill, MA (42.6N,71.5W) measured equatorward neutral winds between 100 and 150 m/s during the

18

night at 300 km and poleward winds between 25 and 50 m/s during the day. Roble et al. (1974), again using the Millstone Hill ISR, measured neutral winds at various altitudes between 250 and 480 km. They, also, measured equatorward winds that averaged 100-150 m/s during the night and poleward winds between 25 and 50 m/s during the day. They found that the equatorward winds maximized between 21 and 01 local time (LT) and then decreased in magnitude toward morning. The neutral winds were also weaker during the winter than during the summer.

Hernandez and Roble (1976) using a Fabry-Perot interferometer at Fritz Peak, CO (40N, 120W) looked at the seasonal variation of neutral winds during quiet times. They found that equatorward winds and temperatures maximized during summer and were at a minimum during winter. Also, the meridional winds were poleward during the day and equatorward at night. Additionally, the zonal winds changed in direction from eastward to westward around local midnight

Hernandez and Roble (1977) also looked at seasonal variations of quiet-time neutral winds. They found that the transition from poleward winds to equatorward winds came earlier in the night the closer it was to summer. However, during winter, the zonal winds did not change from eastward to westward. Winds measured during Sept. 1975 show average equatorward winds of 100-200 m/s (maximizing at midnight) and average zonal winds of 25-50 m/s. During winter, the maximum equatorward winds decreased in magnitude from 100 m/s in October to 20 m/s in December.

Sipler et al. (1981) using a Fabry-Perot interferometer at Laurel Ridge, PA (48.1N,79.2W) measured night time neutral winds for 14 Au-

gust 1980. They found that the neutral temperature decreased from 1500K at 21LT to 1200K at 05LT. The zonal winds changed from 50 m/s eastward at 21LT to zero at 00LT and then became westward. The meridional winds went to zero at 21LT and then became equatorward reaching a maximum of 75 m/s at 00LT. The meridional winds then remained constant until 05LT.

Hernandez and Roble (1984) looked at the changes in the thermospheric F region neutral winds from solar mimimum to solar maximum over Fritz Peak, CO. The measurements spanned the years from 1973 until 1979. Hernandez and Roble found that the observed wind pattern changed from solar min to solar max. First of all, during winter for both solar min and max, the zonal winds blew eastward throughout the night, not reversing to westward until morning. During summer at solar min, the zonal winds would be westward throughout the night averaging 50-100 m/s. While at solar max, winds would be eastward during the early evening, shifting to westward around 21-23LT with a maximum magnitude of 100 m/s. The transition time from eastward to westward winds moved from early morning in winter to early evening in summer.

During solar max, there was a difference between the magnitude of the winds measured north of the observing station, and winds measured south of the station. During summer, winds measured north of the station were 100 m/s larger than winds measured south of the station. During winter, this difference decreased to 50 m/s. The north-south difference was not apparent during solar min. The maximum equatorward winds during solar max ranged from 60 m/s (north of the station) to 30 m/s (south of the station) in winter, and 175 m/s (north) to 75 m/s

20

(south) in summer (maximum equatorward winds in August). This difference was attributed to enhanced auroral heating and ion drag, the influence of which diminishes away from high latitudes. During solar min, the maximum equatorward winds ranged from 75 m/s in winter to 150 m/s in summer.

Sipler et al. (1982) also looked at the variations in neutral winds during solar min and max, with measurements spanning the years 1975 to 1979. Their wind measurements generally agreed with those from Fritz Peak. In addition, they noticed variations in thermospheric temperature. During solar max, the temperature maximized at approx. 1500K in the evening (18LT) and decreased through the night to 1000K at 06LT. During solar min, this pattern varied depending on season. During winter, the temperature decreased from approx. 700K at 17LT to 600K at 02LT. During equinox, temperatures decreased from 900K at 19LT to 600K at 22LT. And during summer, temperatures decreased from 1100K at 20LT to 700K at 23LT.

The quiet-time neutral wind pattern at low-latitudes has been investigated by Harper (1973), Burnside et al. (1981), and Burnside et al. (1983) using a combination of incoherent scatter radar and Fabry-Perot interferometer measurements at Arecibo, Puerto Rico (18N,67W). The observations were generally similar to those at mid-latitudes with zonal winds, eastward in the early evening, transitioning to westward in the early morning hours during summer. During winter, the zonal winds remained eastward through the night, but decreased in strength towards morning. (eg. winds eastward at 125 m/s @21LT decreasing to zero at 04LT.) The meridional winds were typically, 50-100 m/s equa-

torward maximizing at 21LT. However, the meridional winds are compli-
cated by the equatorial midnite temperature maximum. The maximum is
the result of semi-diurnal tides and leads to a density bulge at the
equator. This results in convergence of the normal equatorward winds
and poleward winds from the bulge over Arecibo at 02-03LT.

Hays et al. (1979), using a Fabry-Perot interferometer at College,
Alaska (64.8N,147.8W) measured high-latitude F region neutral winds
during geomagnetic quiet-times. They reported 100 m/s westward winds
in the evening and 100 m/s eastward winds from 00 to 07LT, along with
equatorward winds throughout the night with a maximum of 200 m/s.
They attributed their measurements to ion drag forces, which caused the
neutral particles to follow the magnetospheric convection pattern.
Killeen et al. (1986) using FPI measurements from the DE2 low altitude
polar orbiting spacecraft and measurements from ground-based FPIs also
determined that the high-latitude, neutral winds are the result of
neutrals being dragged along by ions (ion drag) which follow the large
double vortex pattern driven by magnetospheric convection.

In summary, mid-latitude quiet-time meridional winds are poleward
during the day , and equatorward at night. Zonal winds are eastward
in the afternoon, and westward in the morning. This pattern is gener-
ally followed at low-latitudes, except for the effects of the equator-
ial midnite temperature maximum, which gives rise to a poleward wind
at 02-03LT and converges with the normal equatorward winds. At high-
latitudes, the neutral winds follow the magnetospheric convection
pattern.

TABLE: 1. SUMMARY OF QUIET-TIME OBSERVATIONS

1. Meridional winds: Poleward (25-50 m/s) during the day.

   Equatorward (100-150 m/s) at night.

2. Meridional winds change from poleward to equatorward, and
   zonal winds change from eastward to westward at approx.
   local midnight.

3. Neutral temperature decreases at night.

4. Nighttime wind speeds are stronger, and changes in direction
   are earlier in the night during summer than during winter.

5. Neutral winds are stronger, and show greater latitudinal var-
   iation during solar maximum than during solar minimum.

6. Low-latitude winds are similiar to mid-latitudes, but are
   complicated by the equatorial midnight temperature bulge.

7. High-latitude neutral winds follow the magnetospheric
   convection pattern.

Storm Time Neutral Winds and Temperatures

During active geomagnetic periods, energy input at high latitudes
can chanage the neutral wind circulation and thermospheric temperature
considerably. The general characteristics of this disturbed circula-
tion, described earlier, are supported by the following observations
(summarized in Table 2). Hays and Roble (1971) measured neutral winds
during two geomagnetic storms using a Fabry-Perot interferometer. The
first storm from Oct 31 to Nov 1, 1968 was characterized by a stable
red arc. The measured winds were equatorward at 250-300 m/s. The se-
cond storm on the night of May 14-15, 1969 showed a temperature in-
crease from 1400K at 21LT to 1600K at 02LT. The measured winds were
equatorward at 350-400 m/s. In both cases, the equatorward winds were
significantly larger (by a factor of 2) than during quiet-times.

Hernandez and Roble (1976b), at Fritz Peak, looked at four geomag-
netic storms during 1974 using a FPI. They measured equatorward winds
averaging 200 to 300 m/s. For one extremely intense storm (Kp=9), they
measured an equatorward velocity of 640 m/s. The zonal winds averaged
100-200 m/s westward, and didn't exhibit the night-time transition from
east to westward winds so often seen during quiet times. However, when
geomagnetic activity decreased, the zonal winds returned to their
normal quiet-time cycle.

Sipler and Biondi (1979) at Laurel Ridge, made Fabry-Perot inter-
ferometer measurements for the geomagnetic storm of 26 March 1976.
They measured equatorward wind of 200-500 m/s and saw a dramatic in-
crease in temperature from 750K to 1500K. It is important to note that

24

all of these are total wind measurements. The measurements contain the normal diurnal wind variation plus the winds generated by the high-latitude source.

Hernandez and Roble (1978) saw evidence of large scale thermospheric waves, known as Traveling Ionospheric Disturbances (TID). These waves are atmospheric internal gravity waves generated by auroral heating. Roble and Hernandez saw the meridional winds increase sharply in the equatorward direction with a large-wave pattern superimposed on the normal diurnal pattern. The maximum winds were over 300 m/s. A particularly intense storm on 6 July 1974 had equatorward winds of 650 m/s. Zonal winds also increased in the westward direction, reaching speeds as high as 200 m/s. For the 1 April 1976 case, by looking at the time difference from when the wave was seen to the north of the station, and when it was seen south of the station, the disturbance phase speed was determined as 400 m/s. Four hours later, a poleward traveling disturbance with a phase speed estimated at 630 m/s was seen. This was attributed to a disturbance generated in the southern hemisphere auroral zone which had propagated northward.

There was, also, an increase in temperature from 1000K to 1600K with a two-peaked wave-like structure superimposed on a mean increase. Each peak corresponded to the passage of a wave disturbance overhead. The case on 3 May 1976 showed considerably more structure in both wind and temperature measurements. indicating a wavelike structure with a period of 2 hours. Maximum winds reached 400 m/s in the equatorward direction and 200 m/s in the westward direction.

Roble et al. (1978) noticed effects of a gravity wave launched by

25

the 18 Sept 1974 sudden commencement on ionospheric electron density, electron temperature, and ion temperature. The gravity wave passage caused electron density to increase by as much as 40% at Millstone Hill and 50% at Arecibo above quiet-time levels over a 3-4 hour period. Electron temperature decreased 600K in this same period. Ion temperature increased by 50K (5%) over the quiet-time mean.

Mazaudier et al. (1985) using the Saint Santin, France ISR, showed that the thermospheric response to a geomagnetic storm consisted of an initial period of wave activity, followed by a longer lasting meridional wind disturbance with equatorward winds above 120 km, and low velocity poleward winds below. Moreover, they found that there was a time delay of 2-3 hours between the time geomagnetic activity increased and the time winds above Saint Santin responded along with a phase delay with altitude. By subtracting out a mean quiet-time wind profile, they found that the equatorward winds due to the disturbance alone were on the order of 50 m/s. The magnitude, however, depended on the level of geomagnetic activity.

It is these aspects of the thermospheric response to a geomagnetic storm that need to be studied further. In later chapters, a generic storm will be modelled. This will be followed by an attempt to model two of the storms presented in Mazaudier et al.

TABLE: 2. SUMMARY OF STORM-TIME OBSERVATIONS

1. Strong equatorward winds (~300-400 m/s).

2. Strong westward winds (~100-200 m/s).

3. Temperature increase of several hundred degrees K.

4. Large-scale thermospheric waves.

5. A circulation characterized by a period of transient waves
   followed by a mean circulation with equatorward and westward
   winds.

III TWO-DIMENSIONAL THERMOSPHERIC MODEL

One way to check a conceptual model is to use computer simulations. A computer simulation not only predicts the motions of the thermosphere and the resultant electrodynamics, but it can also be used as a tool to learn about and better understand the physics involved. Additionally, perturbations introduced into the simulation can be used to determine the sensitivity of the thermosphere. This yields a better understanding of the interactions that occur in the thermosphere-ionosphere system.

The two-dimensional, time-dependent, thermosphere model of Richmond and Matsushita (1975) was adopted for this study. The model was originally developed to simulate the winds and temperature variations in the thermosphere that result from heating associated with auroral region electric currents during a large hypothetical isolated magnetic substorm. The model was later modified by Blanc and Richmond (1980) to simulate storm-time ionospheric electrical currents.

A two-dimensional model is a simplification of reality. Zonal winds and east-west electric currents are assumed to be longitudinally symmetric. The model is also symmetric about the equator. This eliminates the possiblity of zonal, or hemispheric variations. On the otherhand, a two-dimensional model includes much of the important physics, is easier to setup and run, and the results are easier to interpet than a 3d model. (Three-dimensional thermospheric global circulation models (TGCM) have been developed by Roble at NCAR, and Fuller-Rowell and Rees at Univ. College London. These types of models

28

have become essential to a better understanding of the thermosphere.)

Model Equations

The model uses the nonlinearized equations of thermospheric dynamics to predict winds, temperatures, pressures, electric fields, and electric currents. It is assumed that the acceleration due to gravity (g) is constant and that the thermosphere is hydrostatic. This allows the use of pressure coordinates, thus eliminating density, which varies over 6 orders of magnitude in the thermosphere.
The equations include;

the hydrostatic equation:

$$\frac{\partial(gh)}{\partial p} + \frac{1}{\rho} = 0$$

the mass conservation equation:

$$\frac{1}{a\sin\theta} \frac{\partial}{\partial\theta} (V_\theta \sin\theta) + \frac{\partial\omega}{\partial p} = 0$$

the zonal component (ϕ) of the momentum equation:

$$\frac{\partial V_\phi}{\partial t} = - \frac{1}{a\sin\theta} \frac{\partial}{\partial\theta} (V_\theta V_\phi \sin\theta) + \frac{\partial}{\partial p} (g\tau_\phi - \omega V_\phi) - \left(2\Omega + \frac{V_\phi}{a\sin\theta} \right) V_\theta \cos\theta$$

$$- \frac{J_\theta B_r}{\rho}$$

the meridional component (θ) of the momentum equation:

$$\frac{\partial V_\phi}{\partial t} = - \frac{1}{a\sin\theta} \frac{\partial}{\partial \theta} (V_\theta^2 \sin\theta) + \frac{\partial}{\partial p} (g\tau_\theta - \omega V_\theta) + \left(2\Omega + \frac{V_\phi}{a\sin\theta} \right) V_\phi \cos\theta$$

$$- \frac{1}{a} \frac{\partial(gh)}{\partial \theta} + \frac{J_\phi B_r}{\rho}$$

the energy equation:

$$\frac{\partial \epsilon}{\partial t} = - \frac{1}{a\sin\theta} \frac{\partial}{\partial \theta} \left(V_\theta(\epsilon + gh)\sin\theta \right) + \frac{\partial}{\partial p} \left(g(q + V_\theta\tau_\theta + V_\phi\tau_\phi) - \omega(\epsilon + gh) \right)$$

$$+ \frac{J_\theta E_\theta}{\rho} + Q_0$$

and the equation of state:

$$p = \rho RT = \rho gH.$$

These equations are fairly standard in meteorological hydrodynamics
with the exception of the electrodynamical terms such as JxB in the
momentum equations and J·E in the energy equation. (A list of symbols
can be found in appendix 1.)

Several terms incorporated in the above equations need to be ex-
panded upon. The energy density is:

$$\epsilon = C_p T + \frac{1}{2}(V_\theta^2 + V_\phi^2).$$

The horizontal viscous stress, including molecular and turbulent co-

efficients of viscosity is:

$$\tau = \frac{\mu_m + \mu_t}{H} \, p \, \frac{\partial V}{\partial p} \, ,$$

and the upward heat flux term, including molecular and turbulent heat conduction is:

$$q = \frac{\kappa_m}{C_p H} \, p \, \frac{\partial (C_p T)}{\partial p} + \frac{\kappa_t}{C_p H} \left(p \frac{\partial (C_p T)}{\partial p} - gH \right).$$

The coefficients of viscosity, molecular heat conduction, and turbulent heat conduction are assumed to be functions of only pressure level and are expressed as analytical functions of p that represent typical values (Richmond and Matsushita, 1975). Table 3. lists these values for various heights and represent the inverse time scales at which the atmosphere comes to equilibrium after being perturbed. Also, included in the model equations are the θ and ϕ components of the ionospheric Ohm's law:

$$J_\theta = - \frac{\sigma_1}{\sin^2 I} \left(E_\theta + V_\phi B_r \right) - \frac{\sigma_2}{\sin I} \, V_\theta B_r$$

and

$$J_\phi = -\sigma_1 V_\theta B_r - \frac{\sigma_2}{\sin I} \left(E_\theta + V_\phi B_r \right)$$

(Chapter V deals with this in more detail).

TABLE: 3. VISCOUS AND HEAT CONDUCTION PARAMETERS

Height km	Viscosity s^{-1}	Molecular Conduction s^{-1}	Turbulent Conduction s^{-1}
80	1.14E-5	2.89E-8	5.67E-6
90	1.14E-5	1.66E-7	5.62E-6
100	1.14E-5	7.44E-7	5.43E-6
110	1.13E-5	3.07E-7	4.56E-6
125	9.64E-6	1.14E-5	6.93E-7
150	2.70E-5	3.95E-5	0
200	1.00E-4	1.48E-4	0
250	3.03E-4	5.44E-4	0
300	9.57E-4	1.44E-3	0
350	2.31E-3	3.48E-3	0
400	5.78E-3	8.70E-3	0
450	1.37E-2	2.06E-2	0

Boundary Conditions

The model is two-dimensional in altitude and colatitude and forms a grid that extends from the north pole to the equator, and between 80 and 450 km. Colatitude spacing on the average is in two degree increments but is not constant. It varies between 1.2 and 2.4 degrees, with closer spacing in the auroral zone and wider spacing at the pole and the equator. The closer spacing in the auroral zone allows for a more detailed representation of the area of maximum heating. Altitude is expressed as a dimensionless height variable $Z = \ln(p_o/ p)$ with $Z=0$ at 80 km and $Z=14.4$ at 450 km for a total of 49 levels each 0.3 of a scale height apart.

Also, the horizontal wind velocity, gas energy density, and pressure are held constant at the lower boundary. Finally, V_θ and V_ϕ go to zero at the pole, and at the lower boundary. V_θ goes to zero at the equator. These last two conditions mean that the boundaries act like totally reflecting walls.

Initial Conditions

Now that the basic computational scheme has been presented, details of the set-up and parameterization need to be discussed. Initially, the model thermosphere is at rest. Hence at subsequent times the winds, temperatures, and electric fields and currents are a result of storm inputs. An initial temperature field is prescribed which follows Jacchia's 1971 model atmosphere with an exospheric temperature

33

of 1000K (fig. 5). Additionally, a background heat source (Q_0) is specified. This not an attempt to model heating in the "quiet-time" thermosphere accurately, rather it provides a vertical heat distribution that maintains the initial temperature structure in the absence of auroral heating. Without this heat source the model thermosphere would slowly cool off.

The initial vertical distribution of electron density is another quantity prescribed in the model. In this case, analytical functions of p are used to represent the electron density profile in the E, F1, and F2 regions based upon Saint Santin incoherent scatter radar measurements. This profile displays a dual maximum structure with maxima at 120 km (E region) and 300 km (F region). The profile is constant with latitude and represents background values. (Fig.6.)

Electrical conductivity is calculated using this profile. (See chapter V for a discussion of conductivity.) The Pedersen conductivity (σ_1) and the Hall conductivity (σ_2) are:

$$\sigma_1(z, R, t) = \frac{N(z, \theta, t)e}{B(\theta)} \frac{r(z, \theta)}{1 + r^2(z, \theta)}$$

$$\sigma_2(z, \theta, t) = \sigma_1(z, \theta, t) \, r(z, \theta)$$

where $N(z, \theta, t)$ is the electron density, e is the electron charge, and $r(z, \theta)$ is the collision frequency divided by the electron gyrofrequency. $B(\theta)$ is the dipolar magnetic field which is aligned with the earth's rotational axis.
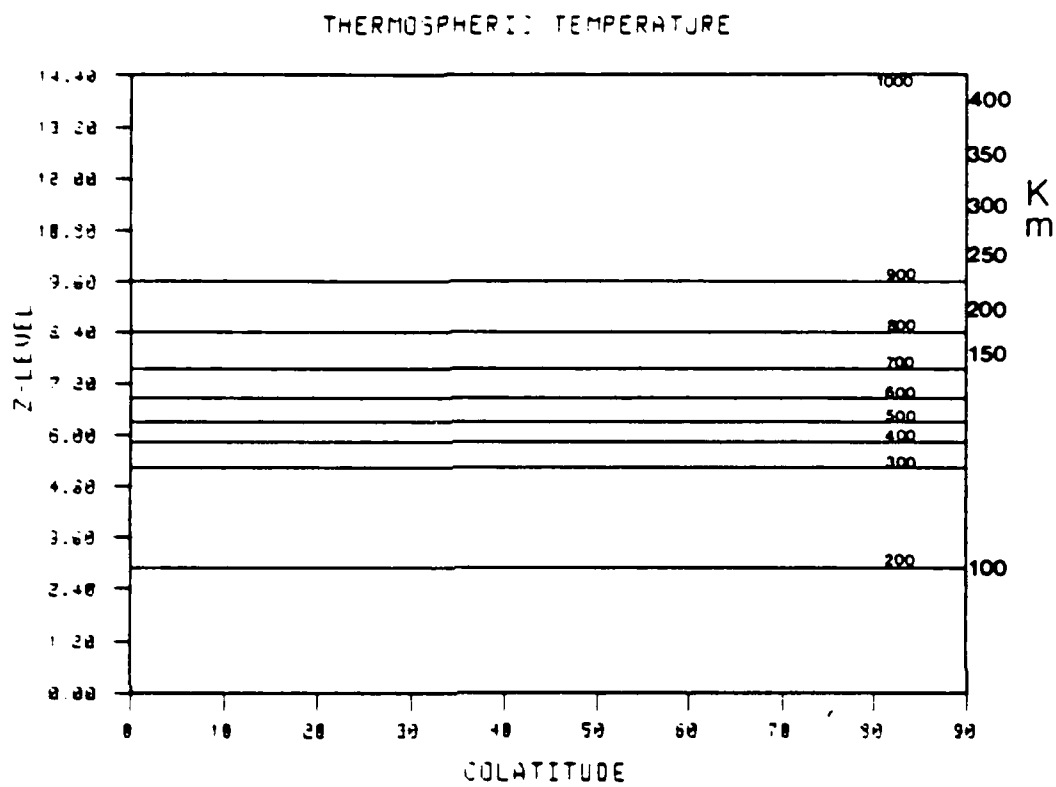
34

THERMOSPHERIC TEMPERATURE

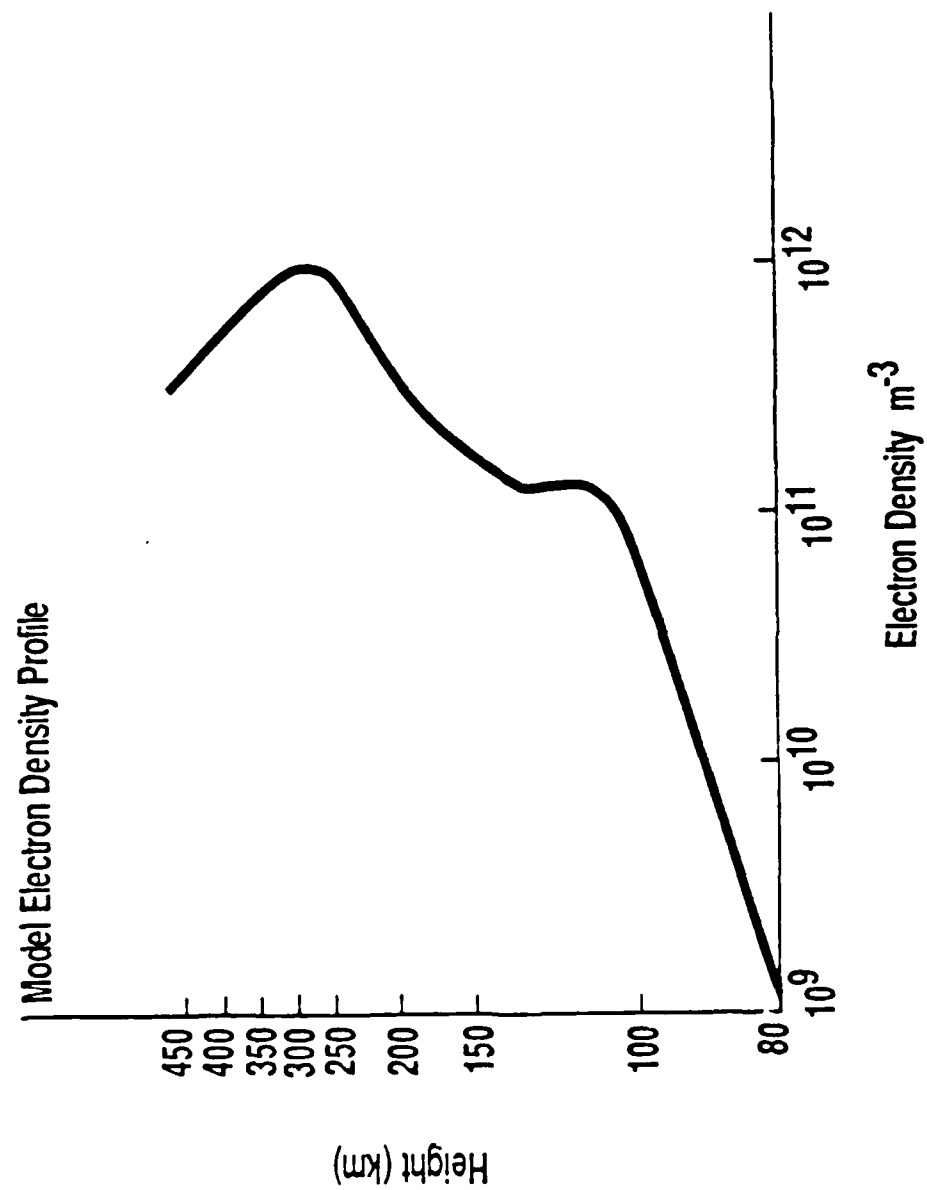Figure S.   Background model temperature profile based on Jacchia (1971).

35

Figure 6. Model electron density profile (electrons per cubic meter).

$$B(\theta) = 5.86 \times 10^{-5} \left[\frac{1}{4} + \frac{3}{4} \cos^2\theta \right]$$

σ_1 and σ_2 are important in the calculation of currents and total power. Values of σ_1 and σ_2 are dependent on both the background electron density and enhancements due to particle precipitation during a storm.

The driving force in the model is the input of energy into the auroral zone. There are three major mechanisms that can provide this energy: Ion drag forces, particle precipitation, and Joule heating. The details of these mechanisms were presented earlier. The goal here is to discuss how they are parameterized in the model.

Ion drag is only weakly coupled to the storm time winds in the model. The appropriate JxB terms are incorporated in the momentum equations, but the electrical conductivity used in the calculation of J doesn't increase during the storm. This is a result of not allowing electron density to increase, and was done because of the zonal symmetry of the model. Typically, during a large storm, such as the one modelled here, the effects of ion drag would switch direction with time as the earth rotates underneath the magnetospheric convection pattern. In a zonally symmetric model there is no direct way to represent local time dependences, so the model provides a background value for ion drag and ignores the storm-time influence.

The model parameterizes particle precipitation by an analytical function but only as it pertains to electron density for Joule heating. Hence, the effect of an enhanced electron density on the overall conductivity, or heating due to the particles themselves is ignored.

Blanc and Richmond (1980) estimated that particle precipitation was small compared to Joule heating. Also, the energetic particles penetrate through the thermosphere to the E region where the density is high and air motions are difficult to initiate.

Joule heating is the most important heat source in the model. How well the model parameterizes Joule heating is therefore crucial. The first question to answer is where does the heating occur? In the thermosphere the maximum heating takes place in the auroral zone. The model parameterizes this spatial characteristic by using a guassian that peaks at 21° colatitude and tails off to zero at the edges of the auroral zone (Figure 7). (The following two paragraphs are from work done with C. Mazaudier and A.D. Richmond, Mazaudier et al.,1987.)

The second question to answer is how to parameterize the magnitude of the Joule heating? One way is to use incoherent scatter radar observations. Incoherent scatter radar measures ion density and ion velocity. From these quantities, electric fields and conductivities can be derived. A direct estimation of Joule heating can be made using the expression $U_j = \sigma_p E^2$, where σ_p is the height integrated Pedersen conductivity and E is the perpendicular electric field. Brekke (1976), Banks (1977), Banks et al. (1981), Vickrey et al. (1982), Duboin and Kamide (1984) provide estimations of Joule heating varying from 2 to 50 ergs $cm^2 s^{-1}$. The problem with using incoherent scatter radar observations is that they only provide Joule heating rates over a small area, and only during the daytime.

A second method of parameterizing Joule heating is by using magnetic data. Global ionospheric electric fields and electric current
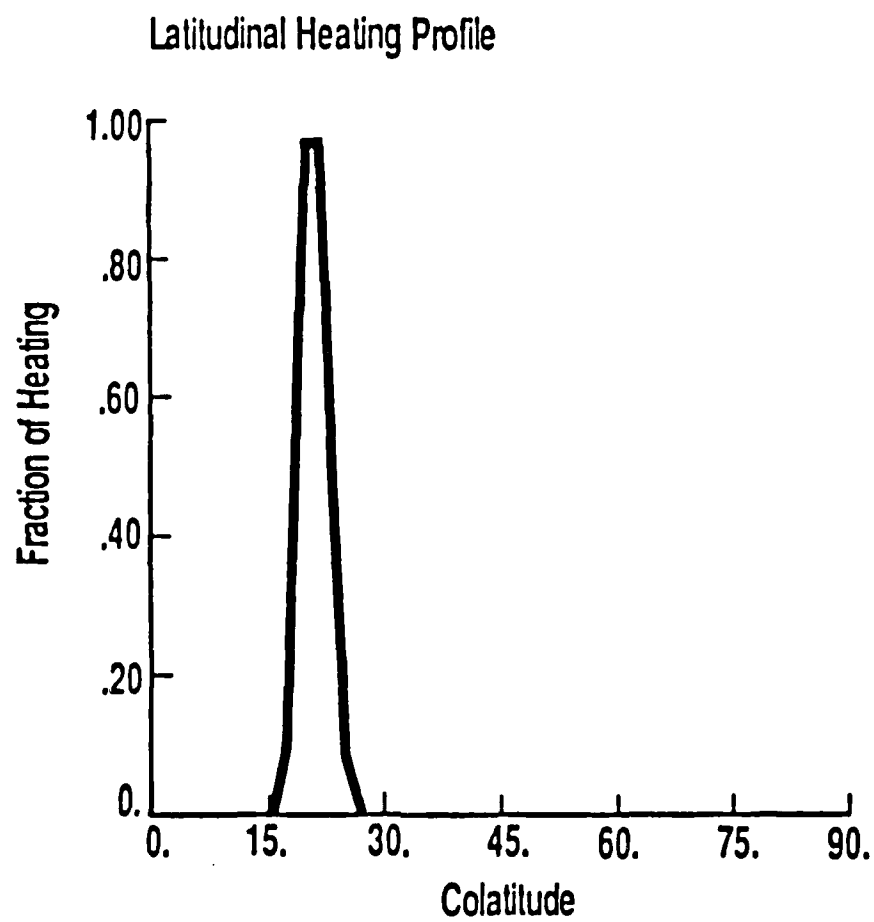
Latitudinal Heating Profile

Figure 7. Latitudinal heating profile. Fraction of heating vs colatitude.

distriburtions can be determined through inversion of magnetic data
(Kamide et al., 1981; Kamide et al., 1982). The electric field and a
conductivity model (Kamide and Richmond, 1982) determine Joule heating.
This estimation of the Joule heating is not as accurate as the estima-
tion from incoherent scatter radar measurements, but it does provide
a global estimate. Comparisons between incoherent scatter estimates
of Joule heating (U_j) and variation of the H component of the magnetic
field $(\Delta H)^2$ at the same location have been made by Brekke and Rino
(1978) and Duboin and Kamide (1984) in order to define a coefficient
h' such that $U_j = h'(\Delta H)^2$. These papers show that the magnitude of
the h' parameter changes with the chosen magnetic event. This under-
scores the point that Joule heating is not simply related to the mag-
netic field variation. Ahn et al. (1983), and Baumjohann and Kamide
(1984) made comparisons between the AE index and Joule heating derived
from magnetic data, in order to define the Joule heating rate integrat-
ed over one hemisphere as a function of the AE index. Table 4. shows
the different expressions found by these authors. The table shows two
formulations of this expression from Ahn et al. based on AE derived
from 71 stations in the first case, and from 12 stations in the second
case. The expression from Baumjohann and Kamide is based on 71 sta-
tions. The main difference between these papers is the conductivity
model that was used. In this study a hybrid expression is used, based
on Baumjohann and Kamide with the factor multiplying the AE index in-
creased by 0.2 to account for the use of AE(12) rather than AE(71).
(In accordance with Ahn et al.) This yields a hemispheric heating rate
of $U_j(12) = 4.0 \times 10^8$ AE(12) Watts.

Ahn et al. 1983 $\qquad$ $U_J = 2.3 \times 10^8 \, AE(12)$ in Watts

Ahn et al. 1983 $\qquad$ $U_J = 1.9 \times 10^8 \, AE(71)$ in Watts

Baumjohann and Kamide 1984 $\qquad$ $U_J = 3.3 \times 10^8 \, AE(71)$ in Watts

Used in Model (Hybrid) $\qquad$ $U_J = 4.0 \times 10^8 \, AE(12)$ in Watts

$AE(12) \rightarrow$ index derived from 12 stations
$AE(71) \rightarrow$ index derived from 71 stations

Table 4. Expressions relating hemispheric Joule heating to the AE index. AE(12) and AE(71) are the Auroral Electrojet Index in nano-teslas based on 12 and 71 stations respectively.

Computational Technique

Two types of computations are made in the model. They are the calculation of flux divergences and the time integration of the dependent variables. Flux divergences are calculated from finite differences. eg:

$$\frac{\partial x}{\partial p} = (x_{i+1} - x_{i-1}) / \Delta p_i$$

where x is a flux and x_{i+1} and x_{i-1} are values of x to either side of where the flux is being calculated. Δp_i is the thickness of the ith pressure layer.

Three quantities are stepped foward in time. They include the meridional wind (V_θ), the zonal wind (V_ϕ) and the energy flux density (ϵ), which is used to predict temperature. The time integration is done as follows (Richmond and Matsushita, 1975):
The momentum equations for V_θ or V_ϕ or the energy equation can be represented by :

$$\frac{\partial \Psi(t)}{\partial t} = F\left[\Psi(t), t \right]$$

where $\Psi(t)$ is V_θ, V_ϕ, or ϵ. This is approximated by:

$$\frac{\Psi(t+\Delta t) - \Psi(t)}{\Delta t} = F\left[\frac{1}{2} \Psi(t) + \frac{1}{2} \Psi(t+\Delta t), t + \frac{1}{2} \Delta t \right] .$$

42

and solved for $\Psi(t+\Delta t)$ by iteration with Ψ^i being the ith iterated value of $\Psi(t+\Delta t)$. The zero iteration is:

$$\Psi^0 (t+\Delta t) = 2 \Psi(t) - \Psi(t-\Delta t).$$

Then:

$$\Psi^1(t+\Delta t) = \Psi(t) + \Delta t \cdot F\left[\frac{1}{2} \Psi(t) + \frac{1}{2} \varphi^{i-1}(t+\Delta t), \ t + \frac{1}{2} \Delta t \right] .$$

Richmond and Matsushita (1975) found that only 2 iterations were needed to converge on an answer and that a time step of 30sec was sufficient to maintain computational stability. For each time step this method is used for each of the quantities at each element of the grid.

IV MODEL RESULTS

In order to simulate the thermospheric response to a geomagnetic storm, an energy input profile was devised to provided an input for the two-dimensional model. The profile, which is shown in figure 8., represents a generic storm. The abrupt switch-on of energy is similar to what would be expected from a sudden storm commencement. This results in an initial period of transient waves, followed by the development of a mean circulation. The storm is maintained at a constant power level of 4×10^{11} Watts, for a period of 12 hours. This is roughly equivalent to a geomagnetic storm with an AE of 1000 for the same period.

The power level of the generic storm represents an average storm. It is on the same order of magnitude as the estimates of Joule heating for the three storms presented by Hernandez and Roble (1978) and the sudden storm commencement discussed by Roble et al. (1978). It falls between values of Joule heating for the "non-storm" of Dickinson et al. (1975) (0.6-1.0$\times 10^{11}$W) and a very strong storm (8.24$\times 10^{11}$W) used by Blanc and Richmond (1980).

What is unusual about this profile, is the period for which this storm is maintained. Typically, observed storms (and most of the modelled storms) have enhancements in Joule heating that last for 3-4 hours. Hence, 12 hours is a long time to maintain this level of heating. Also, a typical storm has a heating rate that fluctuates with a period of 2-4 hours. By maintaining the Joule heating at this rate for 12 hours, the storm-time mean circulation is able to approach a
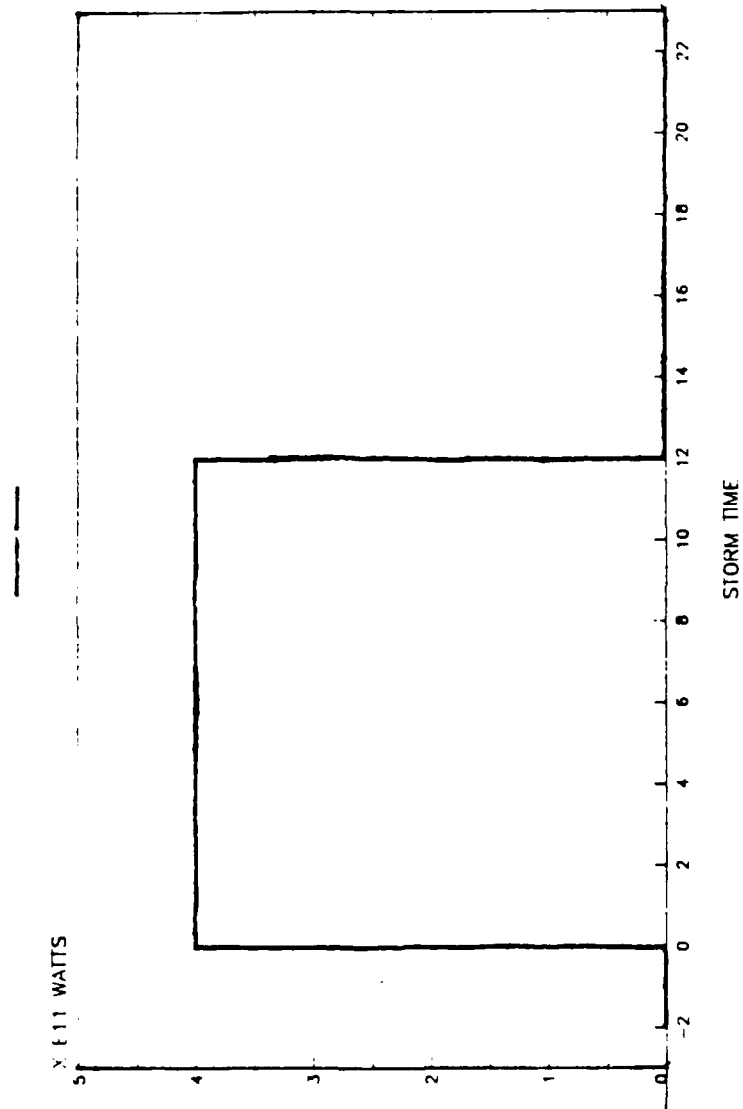
ENERGY INPUT PROFILE

×E11 WATTS

STORM TIME

Figure 8. Generic storm energy input profile.

45

steady-state (although, it still hasn't been reached at this point). The addition of periodicity in the heating profile produces a similar periodicity in the response (eg. a forced oscillator). Although, as Francis (1975) has stated the oscillatory nature of large traveling disturbances does not necessarily imply an oscillatory source. The simple heating profile used here, however, makes it easier to separate out the effects of the transient waves and the mean circulation.

Model Generated Waves

The impulsive heating, which results from this heating profile, initiates strong upward motion that generates waves. These waves show up as a perturbation in the meridional wind field that starts at the heat source in the auroral zone and propagates both poleward and equatorward. Figure 9. shows the propagation of the disturbance for various times at an altitude of 250 km. This altitude was chosen because it was in the middle of the model grid and was the same altitude as the majority of the observations.

The wind disturbance arrives at the equator in 3-4 hours with an amplitude of 55 m/s in the equatorward direction. This is similar to the amplitudes observed by Mazaudier et al. (1985). However, even after subtracting out a quiet-time mean wind, the winds seen by Hernandez and Roble (1978) are still larger by a factor of three. Since the model gives a linear response to heat inputs, it would take a storm three times as large as used here to achieve a similar amplitude. The disturbance also exhibits a phase speed of 524 m/s

46

(@250 km), which is in line with that observed by Hernandez and Roble (1978).

The disturbance is actually a wave packet made up of a whole spectrum of waves (Hines, 1974) of various periods and wavelengths. This makes it difficult to determine a specific period or wavelength. The model-produced waves exhibit a period on the order of 100 minutes and a wavelength between 2000 and 4000 km. The packet appears as a single impulse at the head of the disturbance because the waves that form the oscillatory tail of the packet have been dissipated via thermal conduction and viscosity. (Chimonas and Hines, 1970; and Richmond and Matsushita, 1975.) The waves appear to be increasing in period at lower altitudes and with increasing distance from the source region. This is a consequence of the fact that the angle at which the wave is preferentially launched is dependent on frequency. The longer the period of the wave, the smaller this angle is. Hence, the longer period waves would be predominantly at lower altitudes and distances farther away from the source (Richmond and Matsushita, 1975; Francis, 1975).

The equatorward propagation of the waves can also be seen in terms of a temperature perturbation. Figure 10. shows similar wave features to those seen in the meridional winds, but in this case the amplitude represents a 4% increase in temperature. This is an increase of 38K over an initial temperature of 942K. Roble et al. (1978) showed a similar perturbation in neutral temperature. Also, after the wave has passed, the temperature has increased by 35K at the equator, signifying that the waves have deposited energy at low latitudes.

MERIDIONAL WINDS
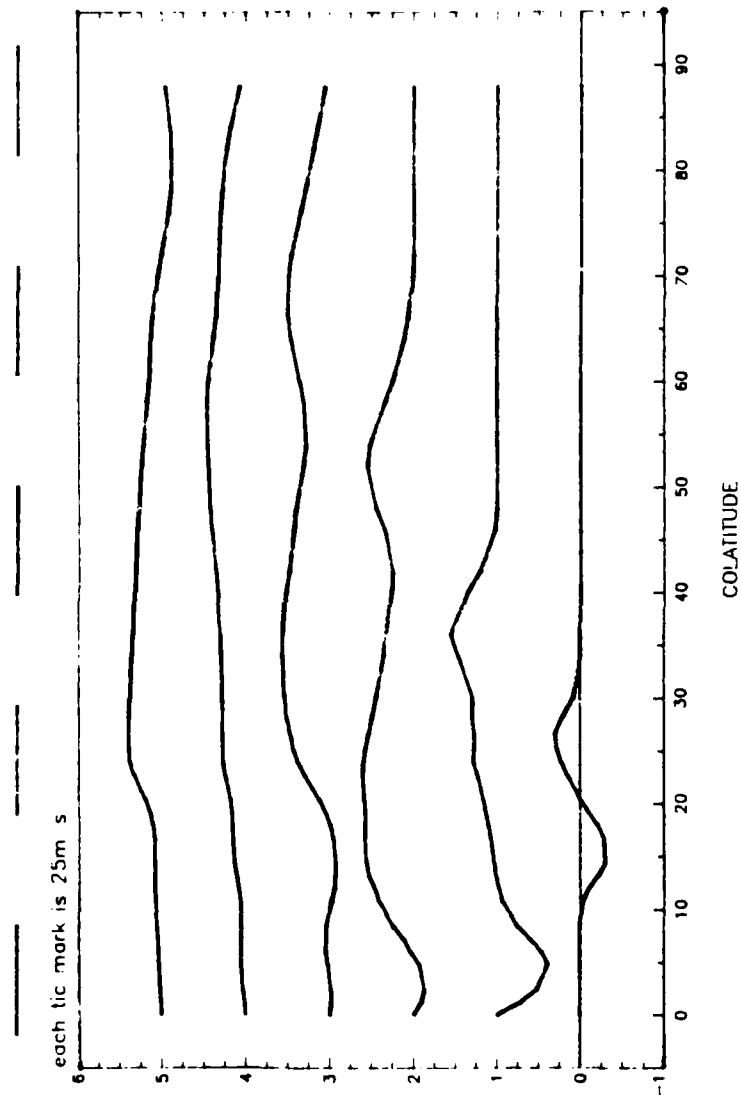AT 250 KM

each tic mark is 25m s

COLATITUDE

Figure 9. Storm generated meridional winds at 250 Km. Storm time (0-5 hrs) vs colatitude is shown. Each tic mark represents 25 m/s, positive southward.
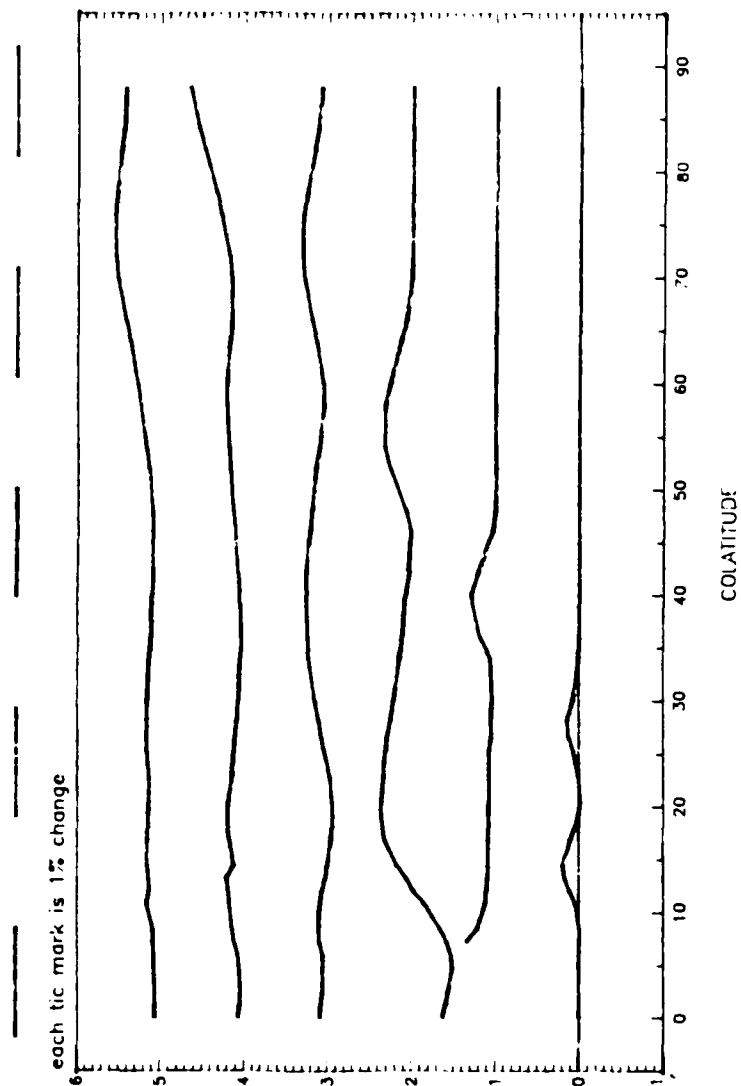
48

Figure 10. Same as Figure 9. except for temperature change. Each tic mark represents 1% temperature change from the initial background temperature (942K).

49

MERIDIONAL VELOCITY

at 48deg colatitude

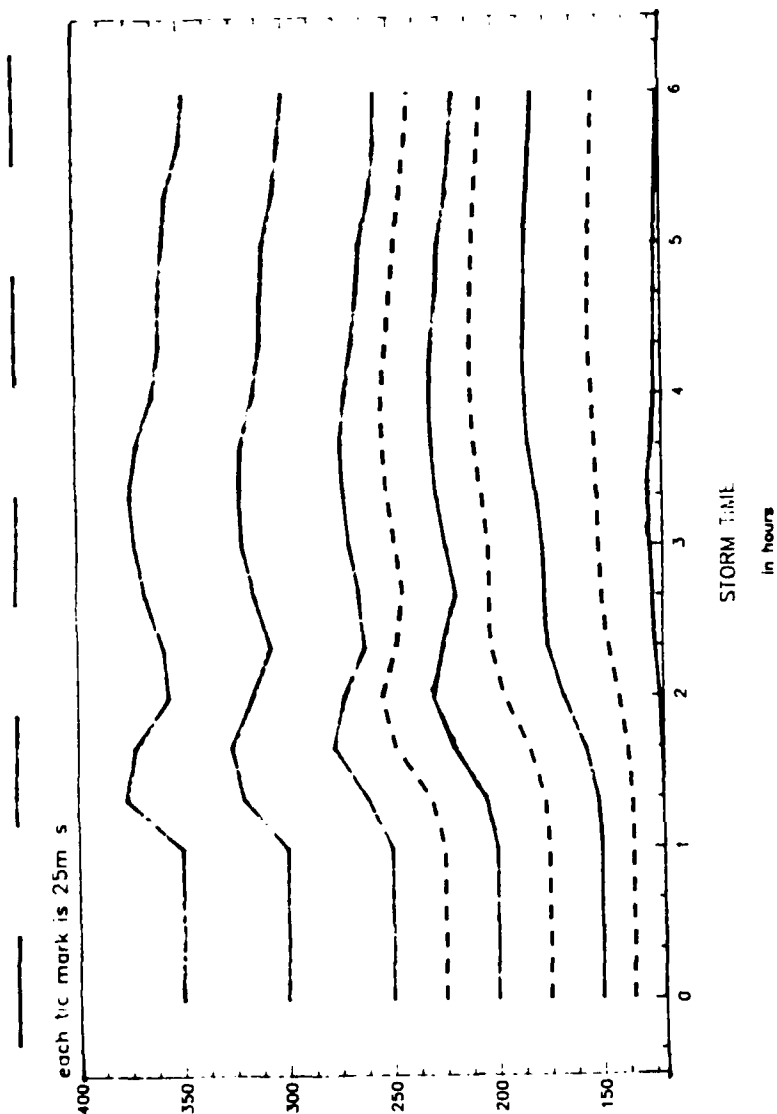each tic mark is 25m s

STORM TIME

in hours

Figure 11. Storm generated meridional winds as seen at 48° colatitude
for various altitudes between 120 and 350 km. Dashed lines are inter-
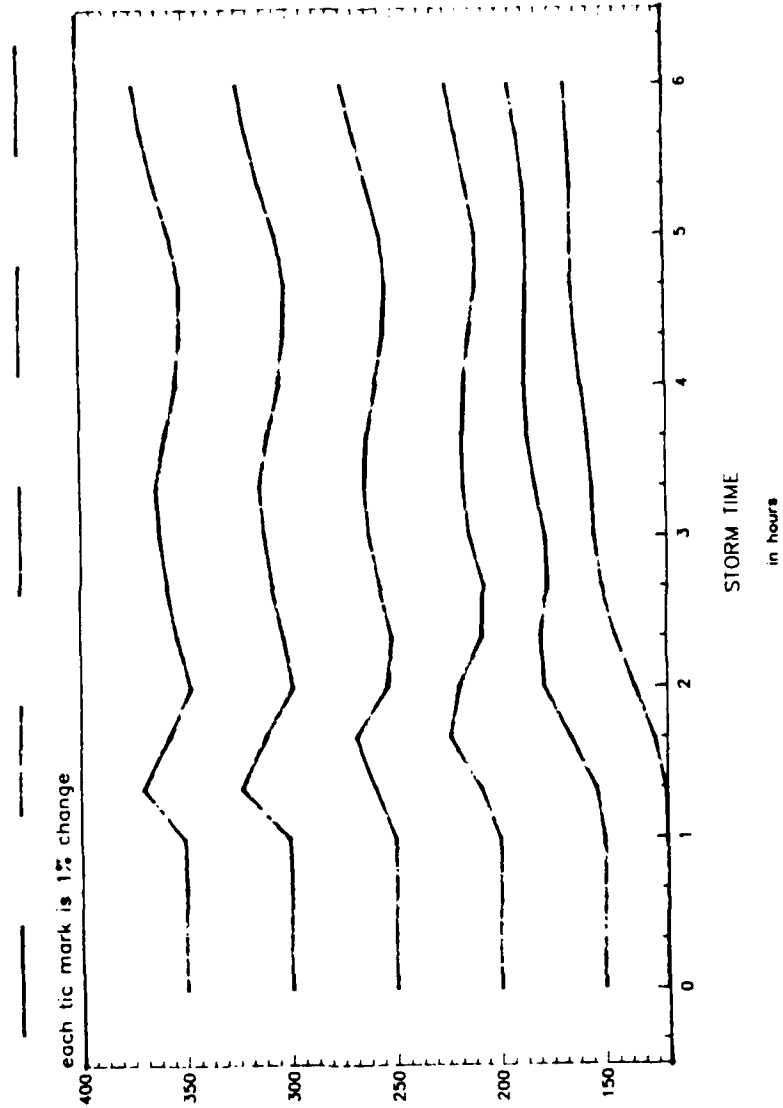mediate altitudes. Each tic mark represents 25 m/s positive southward.

Figure 12. Same as Figure 11. except for temperature change. Each tic mark represents 1% change from the initial background temperature (942K).

51

Figures 11. and 12. show the disturbance as it would be seen at a single colatitude for the meridional velocity and temperature change, respectively. This is how the observing stations would see the disturbance. A colatitude of 48 degrees was chosen because it corresponds to the colatitude at which the majority of the observations are made. Above 250 km, the waves are pretty much in phase with altitude. This is due to the dominant influence of viscosity on the bulk motion of the air. Below 250 km, the waves exhibit a distinct phase lag with altitude; this lag is about 1.66 hours from 250 km to 120 km. This phase lag leads one to believe that the waves are gravity waves. The phase tilt is what is expected of gravity waves with a low altitude source (120 km) and with energy (group velocity) propagating upward (Hines, 1960). Figure 12., also shows that after five hours, there is a general increase in temperature, resulting from the development of the mean circulation.

Mean Circulation

Heating in the auroral zone leads to the development of a pressure bulge at high latitudes and hence a pressure gradient that drives horizontal winds. Initially, there is a period of transient gravity waves as described in the previous section. After these waves have passed through the system, a mean circulation developes.

Figures 13a,b, and c show the model outputs for the meridional, zonal, and vertical components of the thermospheric wind, respectively, two hours into the simulation. Figure 13d, shows temperature changes,

52

also after two hours. (It is important to note that the transient waves are evident at two hours; however, the beginnings of the mean circulation can also be seen at this time.)

Figure 13a shows that the leading edge of the wind disturbance has reached 70° colatitude at the upper boundary of the model. At lower altitudes, the disturbance lags behind this. Just equatorward of the auroral zone, the developing circulation is confined between the altitudes of 120 and 200 km, and between colatitudes of 22.5° and 45° with maximum equatorward winds of 110 m/s. Poleward of the auroral zone, there is a smaller poleward wind with maximum winds of 30 m/s. Above 200 km, the transient gravity waves (as described earlier) are dominant.

Figure 13b, shows the zonal winds at the two hour point. These winds are the result of the coriolis force acting on the meridional winds. Ion drag forces, as shown by Richmond and Matsushita (1975), would also affect the zonal component of the winds. However, ion drag forces are suppressed in this version of the model for reasons discussed earlier. Westward zonal winds extend from 22.5° to 45° colatitude above 120 km with a maximum of 50 m/s. Poleward of the auroral zone, there are eastward zonal winds, which reach a maximum of 40 m/s.

The vertical component of the wind (Figure 13c) at this time shows a core of upward moving air centered about 21° colatitude with maximum vertical velocities of 8 m/s. Equatorward of this core to 76° colatitude, the vertical motion is downward with velocities less than 1 m/s, except above 200 km where gravity wave activity is present.

Figure 13d shows a temperature increase over the model's initial

temperature field. There has been a significant temperature increase in the region between the pole and 40° colatitude, and between 110 and 170 km. The maximum increase is 110K at 135 km between the pole and the auroral zone. At 40° colatitude, the temperature has increased 40K at 135 km. The temperature increase is the consequence of Joule heating at E region heights in the auroral zone, which the winds then transport away from the source. Above 200 km, and centered about the auroral zone is another region of increasing temperature. This increase is the result of Joule heating at F region heights and has reached 70K after two hours. Above 200 km, temperature perturbations are associated with the transient gravity waves are seen. Figure 13d, also shows the equatorward extent of the disturbance (colatitude 70° at the model's upper boundary).

Figure 14a shows that after 5 hours, the effects of the mean circulation, centered about 150 km, have reached the equator. Just equatorward of the auroral zone (25° colatitude), the maximum equatorward winds are 130 m/s. At mid-latitudes, the winds are equatorward at 50-70 m/s, which is in reasonable agreement with Mazaudier et al. (1986) and other storm-time observations (once a quiet-time mean is subtracted). At low latitudes, the equatorward winds are 10-30 m/s. Notice also, that the winds seem to be confined to heights above 120 Km. This is due to the higher air density below 120 km. In fact, a weak poleward wind developes (less than 10 m/s) at the lower altitudes to satisfy the need to conserve mass in the system (a return flow).

Above 240 km, the effects of the waves have weakened, but are still evident. At 5 hours, there appears to be a poleward propagating wave

at low latitudes. This wave is an artifact of the model boundary conditions. Since V_ϕ must go to zero at the equator, the equatorward boundary acts like a reflecting wall. Hence, waves that were originally propagating toward the equator are reflected back towards the pole. Some physical significance can be attached to this reflected wave. It represents a wave that was generated in the southern hemisphere's auroral zone and has propagated northward into the northern hemisphere.

After 5 hours, the westward winds have expanded equatorward to 76° colatitude and the maximum speed, located at 150 km and 34° colatitude, has increased to 120 m/s (figure 14b). The vertical velocities (figure 14c) show that the wave activity has all but disappeared, leaving a "jet-like" core of upward vertical motion centered at 21° colatitude. This core exhibits a double-maxima structure, one in the E region (with a max wind of 4 m/s) and one in the F region (with a max wind wind of 8 m/s). Elsewhere, the vertical winds are predominately downward with velocities less than 1 m/s. Also, at this time, the temperature at low latitudes has increased by 20-60K. In the auroral region at 130 Km, the temperature has increased by 140K (figure 14d).

Three hours later, after the storm has been going for 8 hours, the meridional winds have maintained their maximum speed but their spatial extent seems to have decreased (figure 15a). This may be due to the fact that the initial temperature gradient (which is driving the winds) has been changed by the winds themselves and the circulation is now readjusting. The zonal winds (figure 15b) have continued to increase in magnitude with a maximum of 140 m/s. Their horizontal extent has

55

also increased equatorward to 77° colatitude. The vertical velocities have increased slightly in magnitude (figure 15c), and the temperature at high latitudes has increased by as much as 160K while at low latitudes it has increased by 60K (figure 15d).

After 11 hours, the mean circulation approaches a steady-state (although, it hasn't been reached yet). The meridional winds (figure 16a) has changed little over the last three hours, except they have expanded in spatial extent slightly. The zonal and vertical winds have changed little over the last three hours (figure 16b,16c). A small area of eastward winds has developed equatorward of the auroral zone and below 120 km. This may be associated with the coriolis force acting on the low altitude poleward winds (the return flow).

Finally, figure 16d shows that the thermospheric temperature in the auroral zone has increased by as much as 200K. At low latitudes temperatures have increased by as much as 100K due to dynamically transported heat from the auroral zone to the equator.
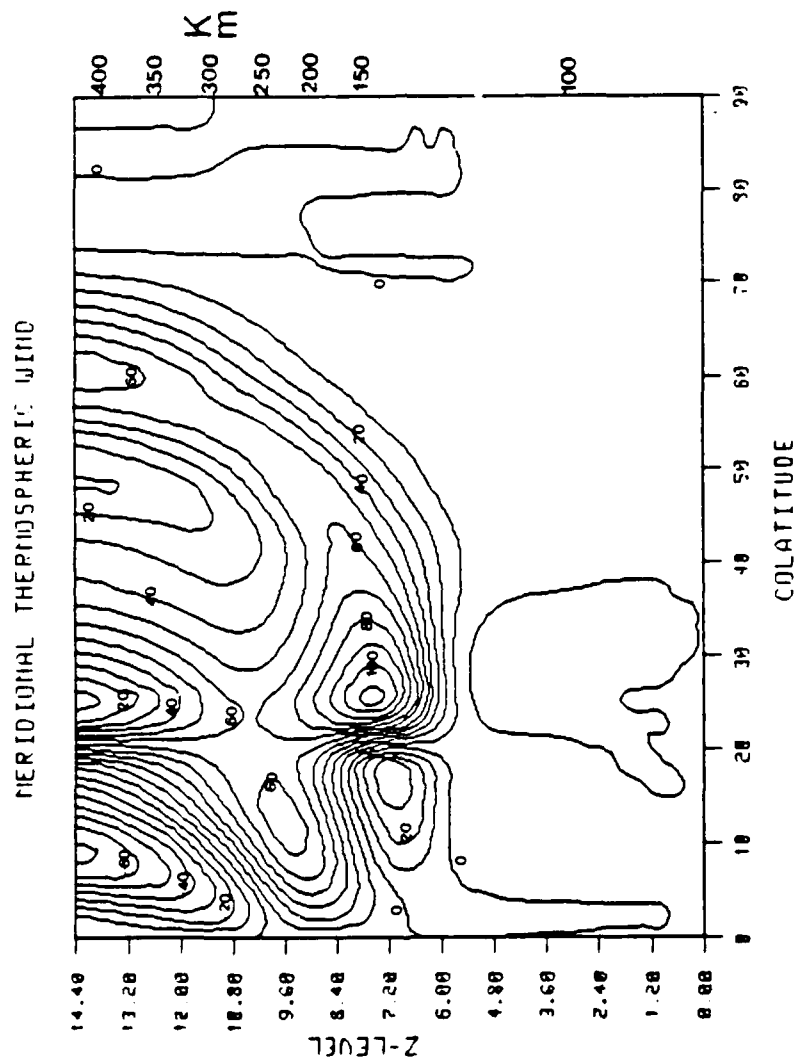
Figure 13a. Meridional winds (positive equatorward) 2 hours into storm simulation. Contours are in 10 m/s increments.
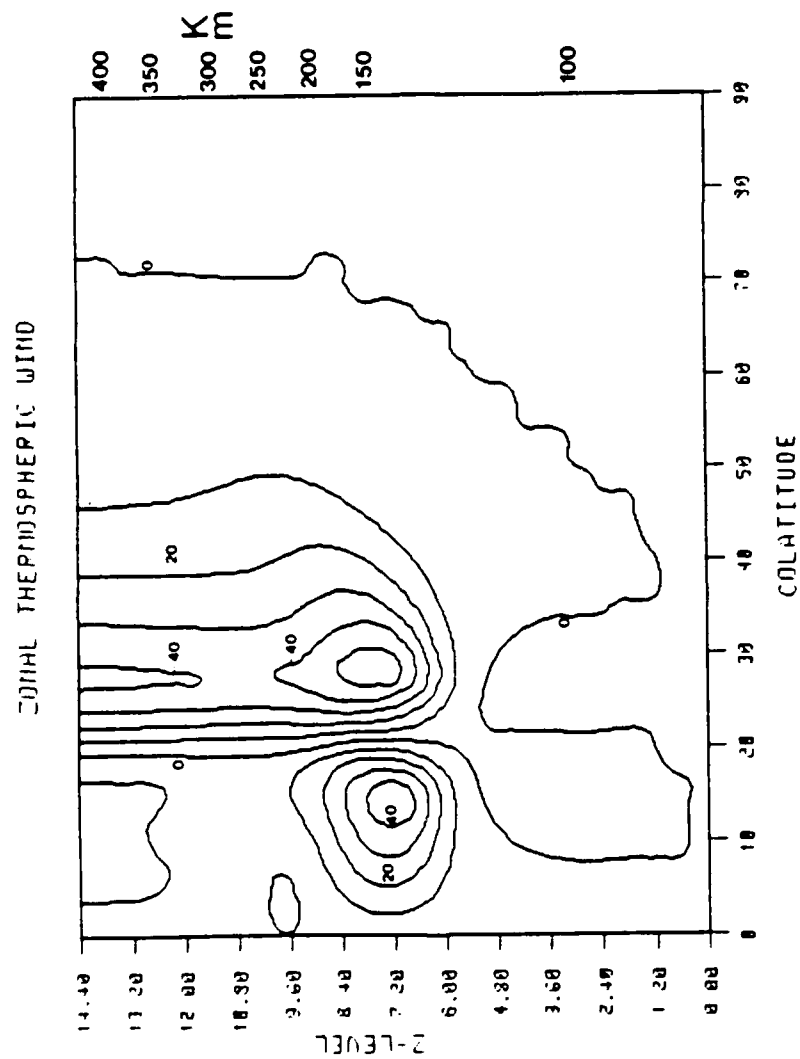
Figure 13b. Zonal winds (positive eastward) 2 hours into storm simulation. Contours are in 10 m/s increments.
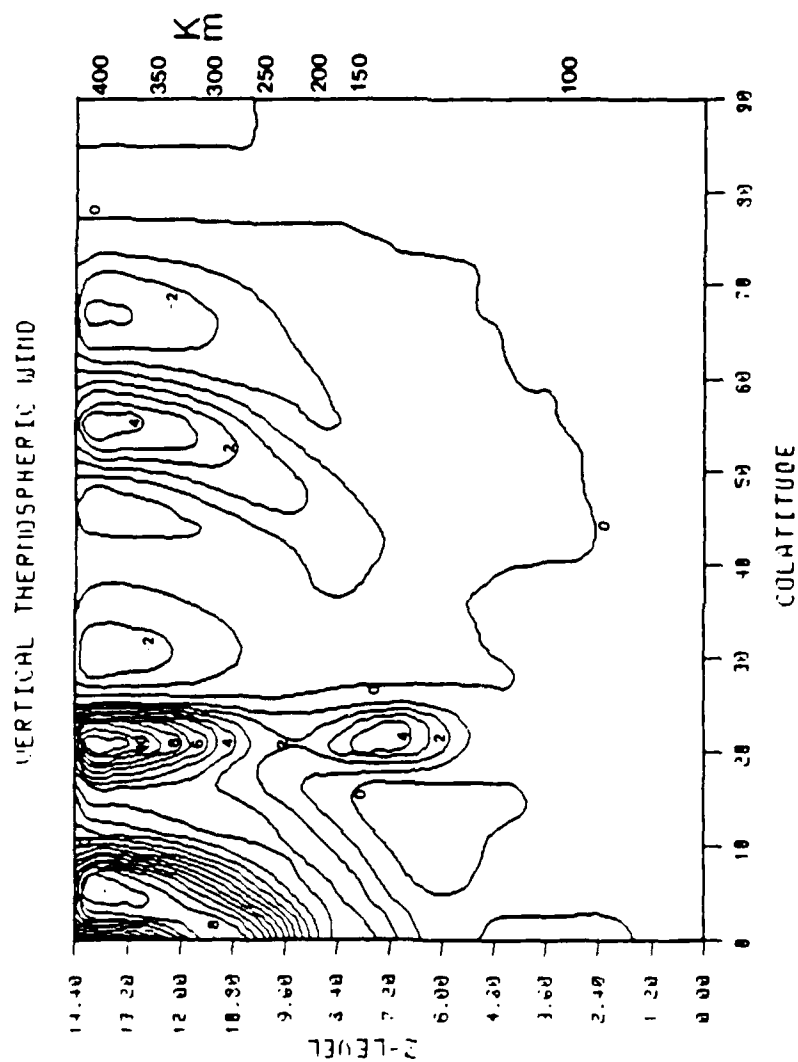
Figure 13c. Vertical velocities (positive upward) 2 hours into storm
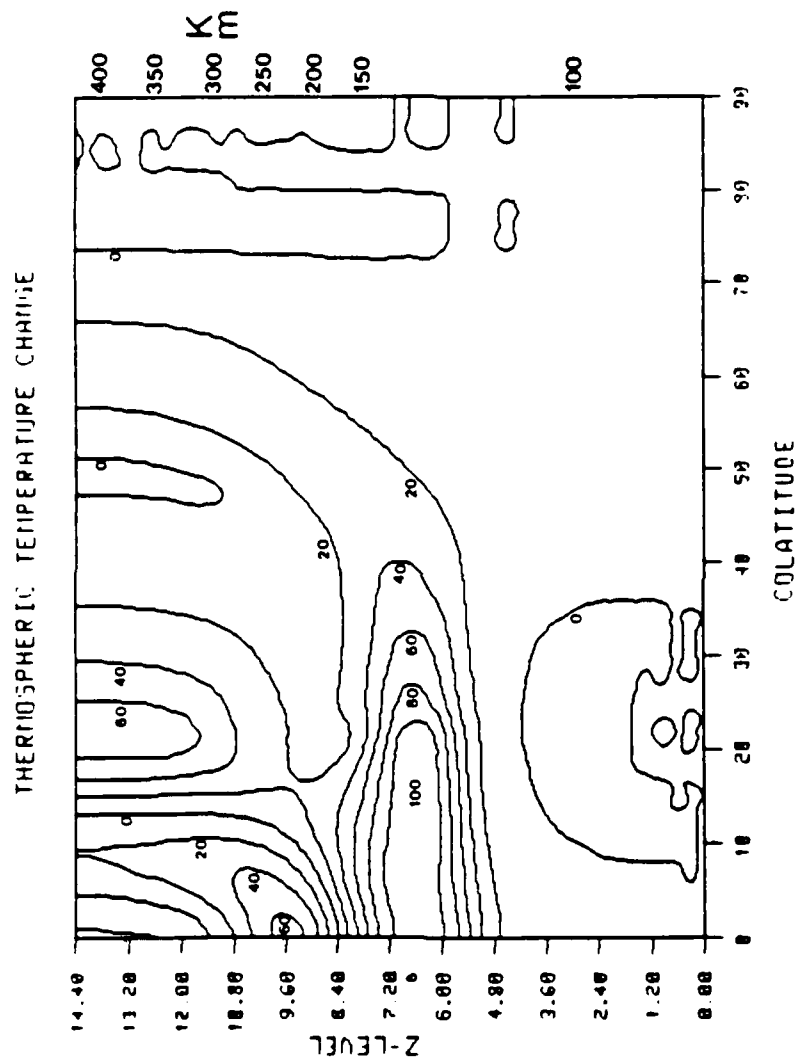simulation. Contours are in 1 m/s increments.

Figure 13d. Temperature change 2 hours into storm simulation.
Contours are in 20K increments.
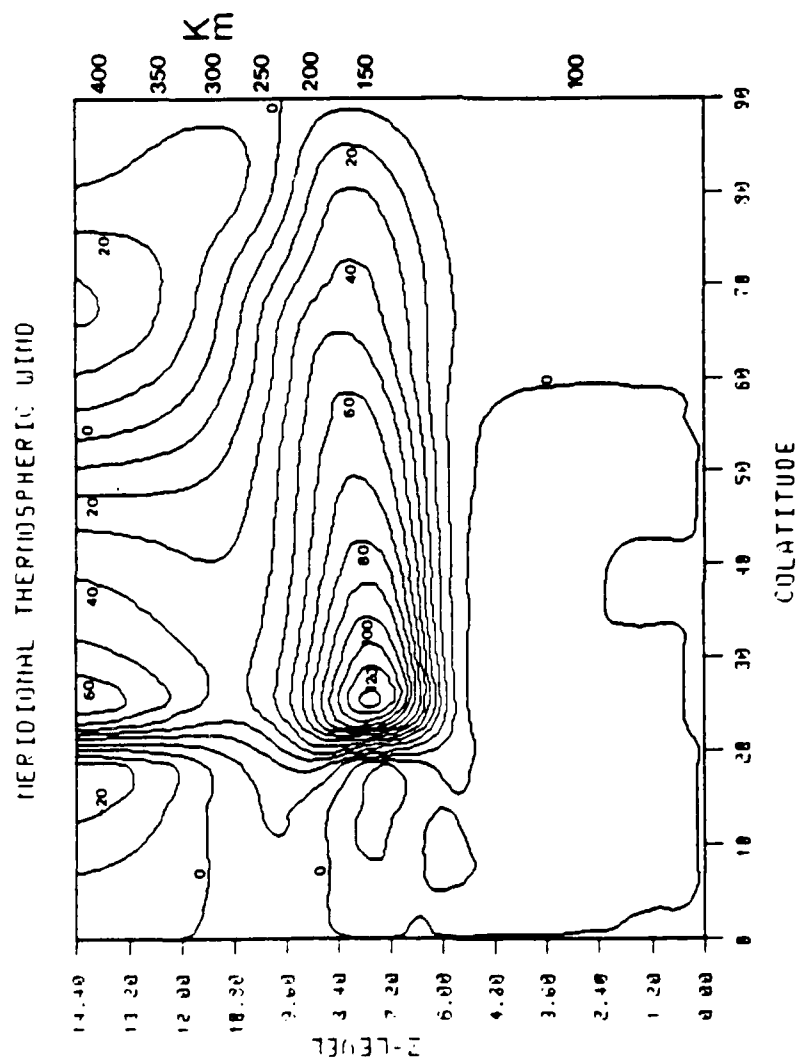
Figure 14a. Same as Figure 13a., except at 5 hours.

Figure 14b. Same as Figure 13b., except at 5 hours.

Figure 14c. Same as Figure 13c., except at 5 hours.

Figure 14d. Same as Figure 13d., except at 5 hours.

64

Figure 15a. Same as Figure 13a., except at 8 hours.

65

Figure 15b. Same as Figure 13b., except at 8 hours.

Figure 15c. Same as Figure 13c., except at 8 hours.

67

Figure 15d. Same as Figure 13d., except at 8 hours.

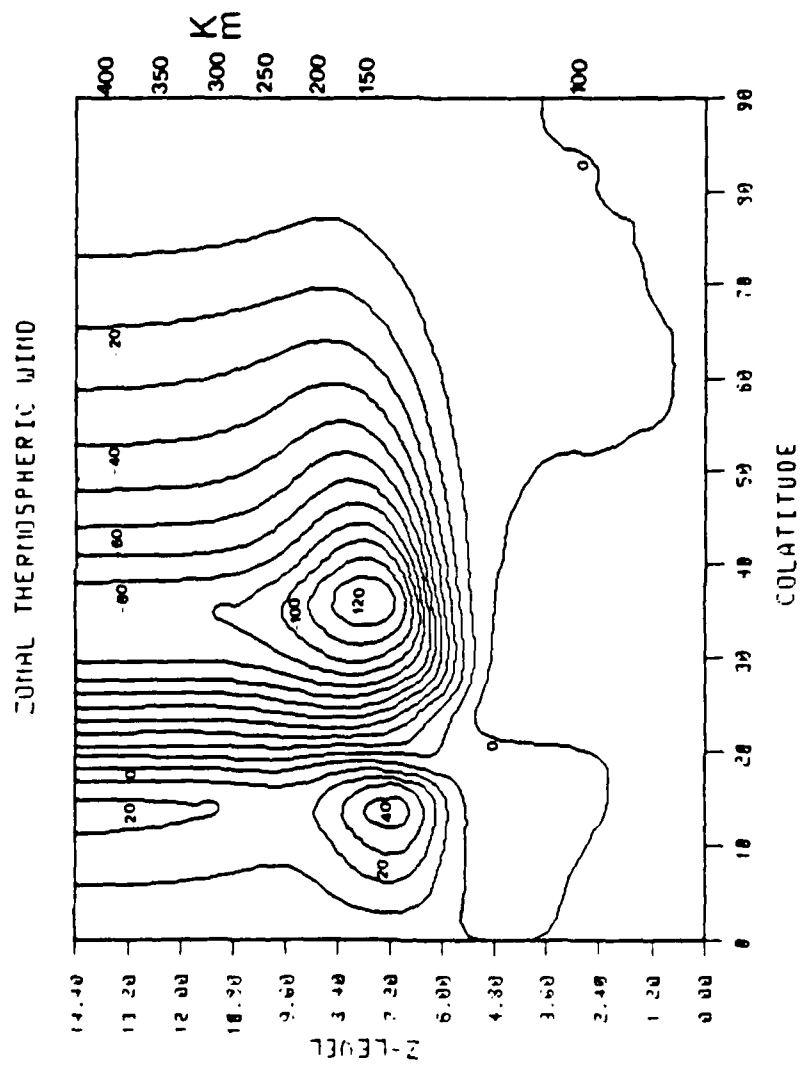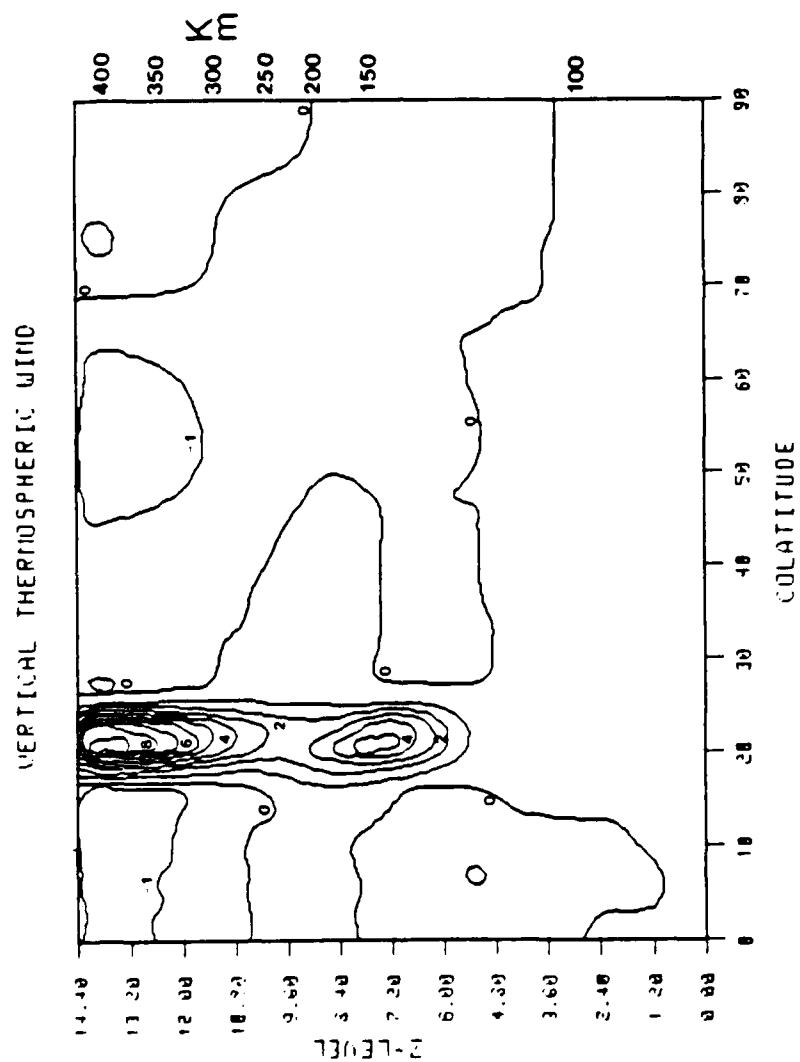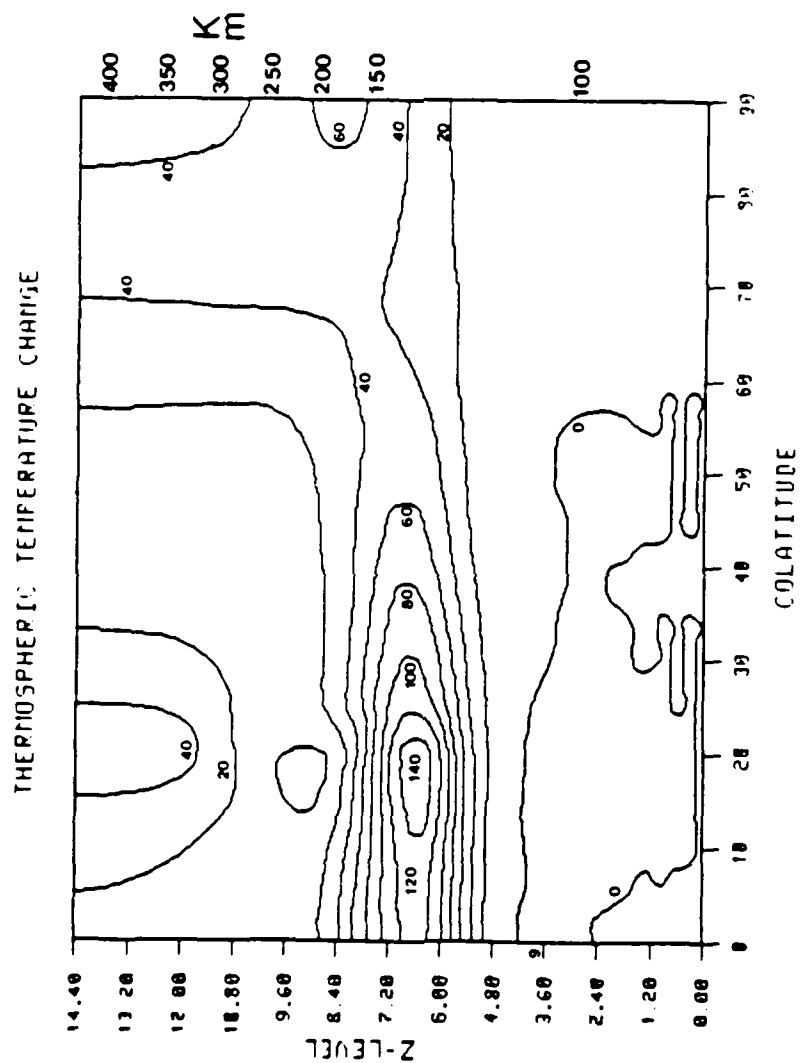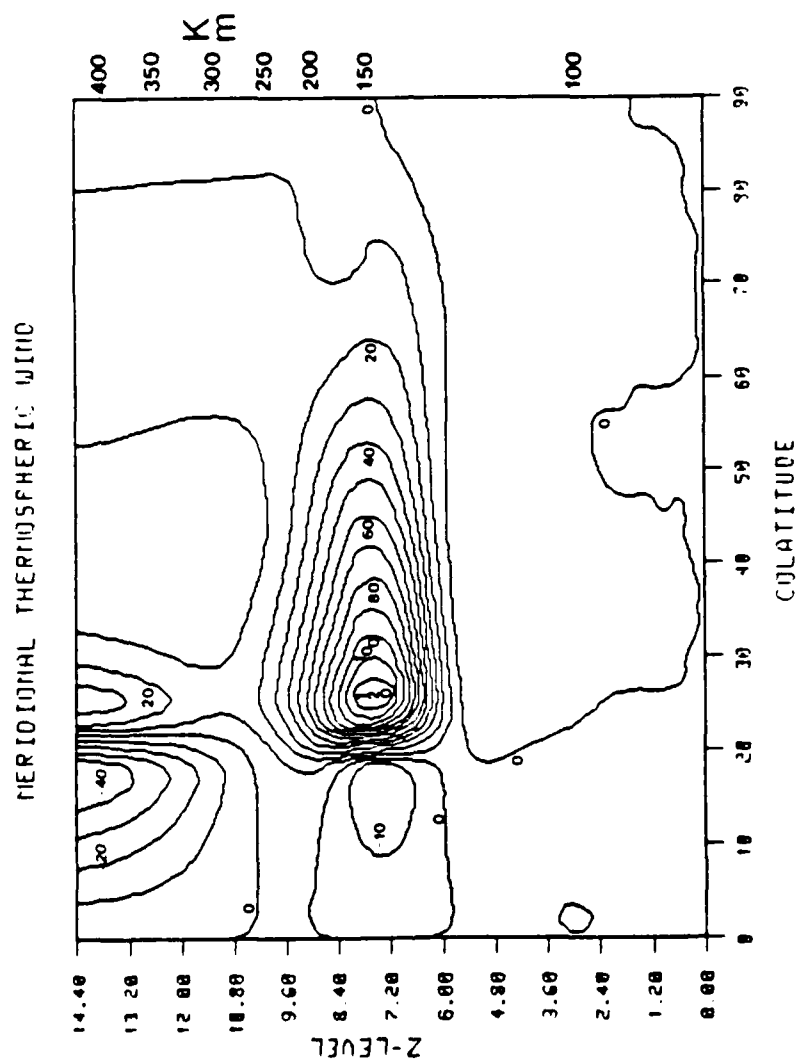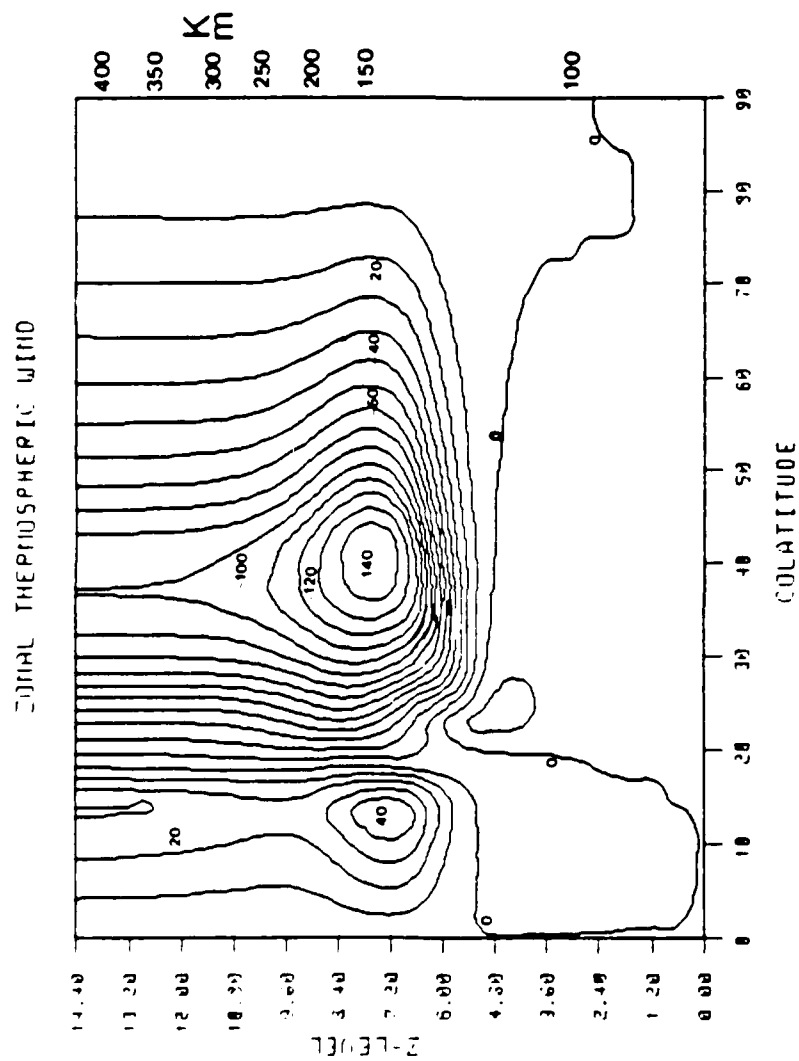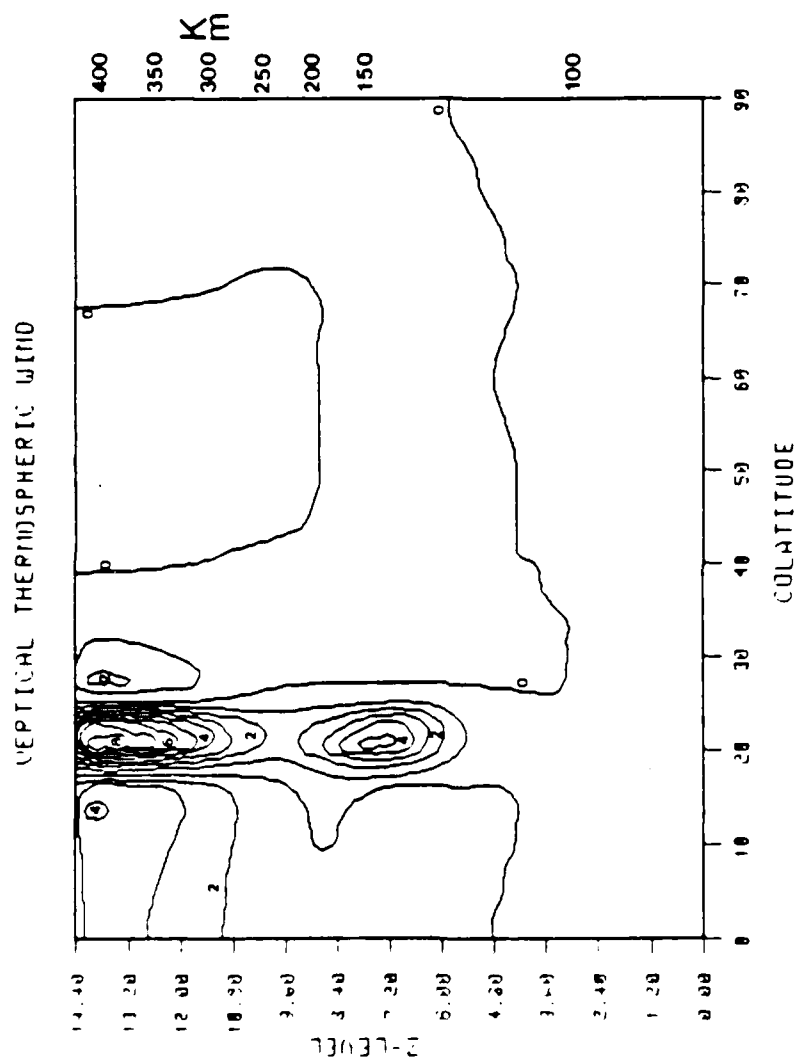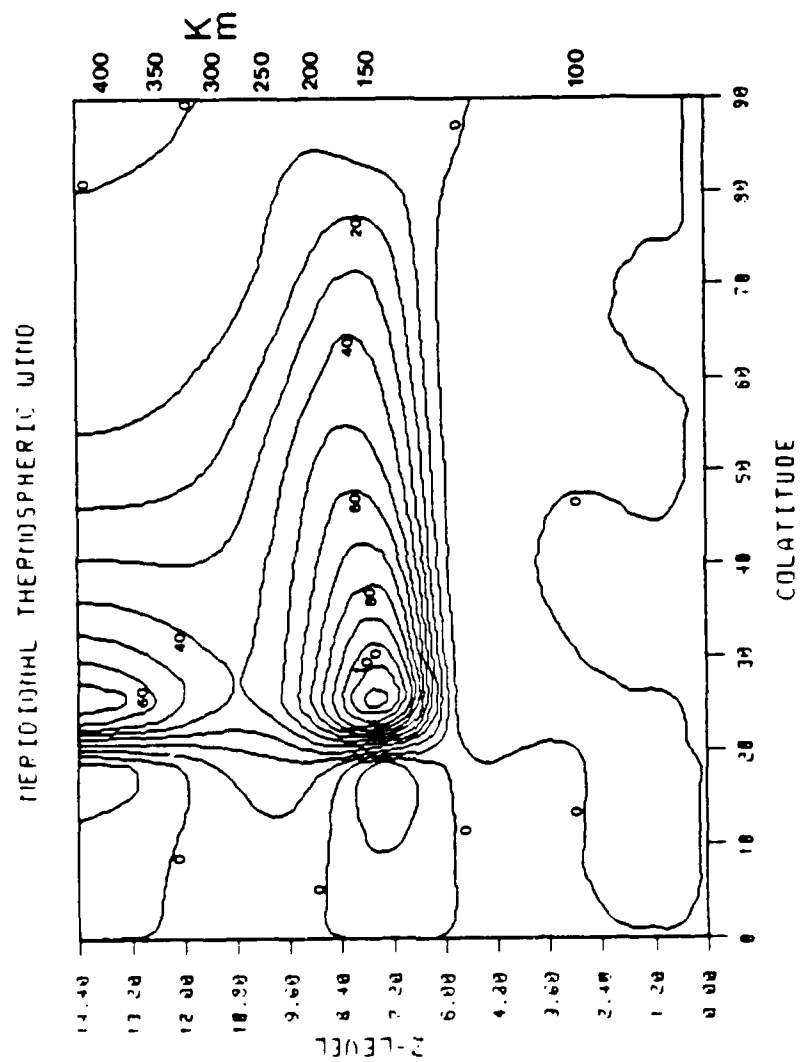Figure 16a. Same as Figure 13a., except at 11 hours.

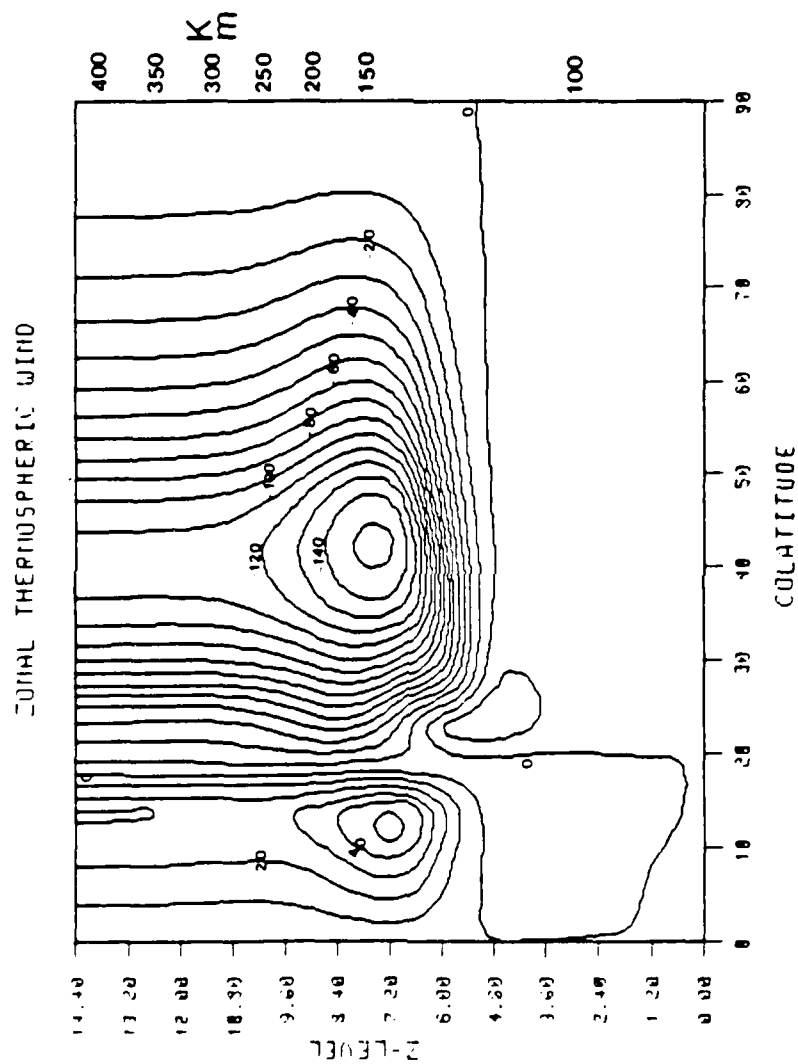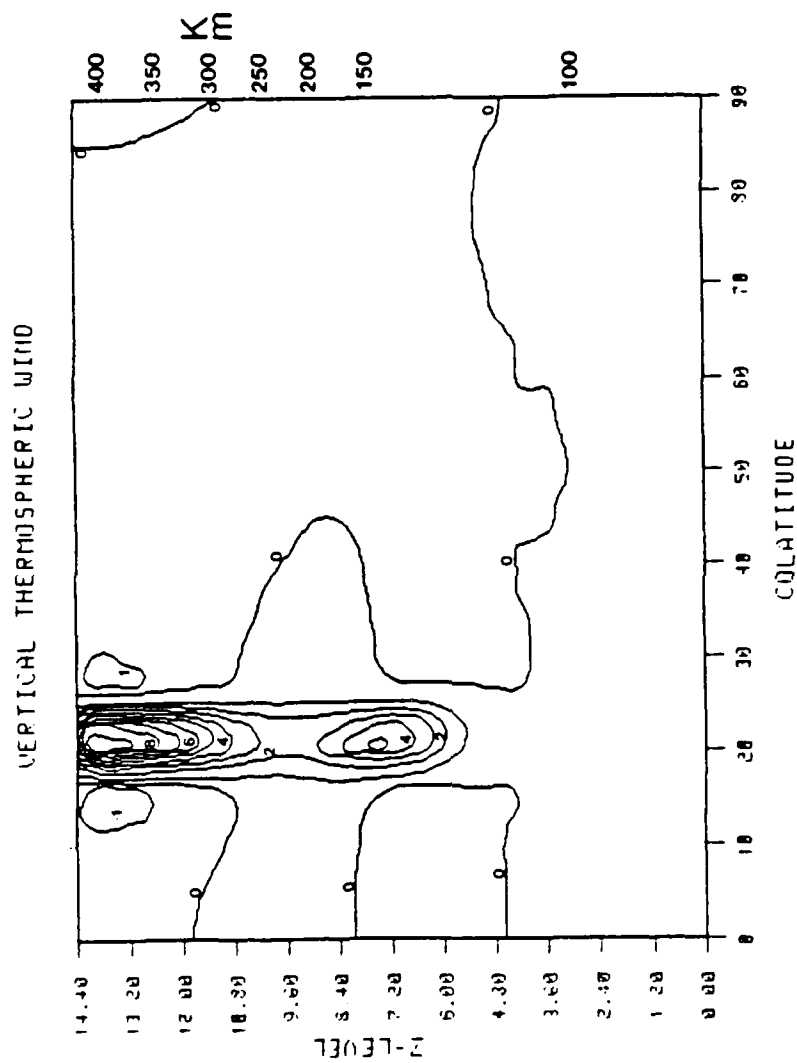Figure 16b. Same as Figure 13b., except at 11 hours.

70

Figure 16c. Same as Figure 13c., except at 11 hours.

Figure 16d. Same as Figure 13d., except at 11 hours.

V ELECTRODYNAMICS

Thermospheric winds move charged particles in the ionosphere through the earth's magnetic field. This results in the generation of electromotive forces which drive electrical currents, and set up electric fields (Richmond, 1979a).

In general, moving charged particles are acted upon by the magnetic Lorentz force ($-q \vec{V} \times \vec{B}$) and gyrate around magnetic field lines. This restricts the movement of particles in the direction perpendicular to field lines. Motion along the field lines, however, is not acted upon by magnetic forces and charged particles therefore can easily move along them.

A force is required to move charged particles across field lines. A perpendicular electric field imposes such a force. At altitudes above 180 km, both electrons and ions move together with the $\vec{E} \times \vec{B}$ drift. Since there is no charge separation, there is no current. Below 80 km, frequent collisions between charged particles and neutrals cause the charged particles to move together with the neutral wind, and again there is no current. Above 80 km, electrons, because of their small size and mass, undergo few collisions and move with the $\vec{E} \times \vec{B}$ drift. Ions, on the otherhand, have frequent collisions, which cause their motion to deviate from the $\vec{E} \times \vec{B}$ direction. Collisions affect ion motion in two ways. First, they stop an ion's foward motion, which allows the electric force to accelerate the ion in the direction of the electric field. The ion now has components of motion in the $\vec{E} \times \vec{B}$ direction and in the direction of $\vec{E}$. This causes charge

73

separation (as the electrons move only in the $\vec{E} \times \vec{B}$ direction) and a Pedersen current in the direction of $\vec{E}$ flows. Second, collisions retard the ion's motion in the $\vec{E} \times \vec{B}$ direction relative to the electrons, causing charge separation and a Hall current in the $-\vec{E} \times \vec{B}$ direction (the electrons "carry" the current).

The currents can be summerized by ionospheric Ohm's law:

$$\vec{J} = \sigma_0 \, \vec{E}_\| + \sigma_1 \, (\, \vec{E}_\perp + \vec{V} \times \vec{B} \,) + \sigma_2 \, \hat{b} \times (\, \vec{E}_\perp + \vec{V} \times \vec{B} \,)$$

The first term is the parallel current, where σ_0 is the parallel conductivity. The second term is the Pedersen current, where σ_1 is the Pedersen conductivity. The third term is the Hall current, where σ_2 is the Hall conductivity and $\hat{b}$ is the unit vector in the direction of $\vec{B}$.

Conductivity relates to the mobility of charged particles, and is dependent on the ratio of the collision frequency (ν) to the gyrofrequency (ω). The parallel conductivity is :

$$\sigma_0 = \left[\frac{N_e}{m_e \nu_e} + \frac{N_1}{m_1 \nu_1} \right] |e|^2$$

The parallel conductivity increases with altitude and quickly becomes large. This allows currents to flow along field lines, which shorts out $\vec{E}_\|$. Hence, this term can be ignored in ionospheric Ohm's law. Additionally, the field lines act like equipotentials and $\vec{E}$ imposed by the magnetosphere can be mapped down to the ionosphere.

The Pedersen and Hall conductivities are:

74

$$\sigma_1 = \left[\frac{N_e}{m_e \nu_e} \left(\frac{\nu_e^2}{\nu_e^2 + \omega_e^2} \right) + \frac{N_1}{m_1 \nu_1} \left(\frac{\nu_1^2}{\nu_1^2 + \omega_1^2} \right) \right] |e|^2$$

and

$$\sigma_2 = \left[\frac{N_e}{m_e \nu_e} \left(\frac{\nu_e^2}{\nu_e^2 + \omega_e^2} \right) - \frac{N_1}{m_1 \nu_1} \left(\frac{\nu_1^2}{\nu_1^2 + \nu_1^2} \right) \right] |e|^2$$

respectively. The Pedersen conductivity maximizes at 140 km, where $\omega_1 = \nu_1$, and is in the direction of $\vec{E}$. The Hall conductivity maximizes at 105 km, where $\omega_1 \nu_1 = \omega_e \nu_e$, and is in the $\vec{B} \times \vec{E}$ direction. Pedersen and Hall currents then arise from either an electrostatic field or an induced electric field, as described by ionospheric Ohm's law.

The quiet-time diurnal and semi-diurnal tidal motions of the thermosphere drive electrical currents. These currents make up the Sq current system, and can be determined from ground-level magnetic variations(fig 17). On the dayside, the result is two large current vortices. In the northern hemisphere, the current flows counterclockwise, and in the southern hemisphere the current flows clockwise. The maximum current is on the order of 6×10^4 Amps. On the nightside, where the conductivity is lower, the currents are half the strength of the dayside currents, and flow in the opposite direction.

Disturbance Dynamo Model

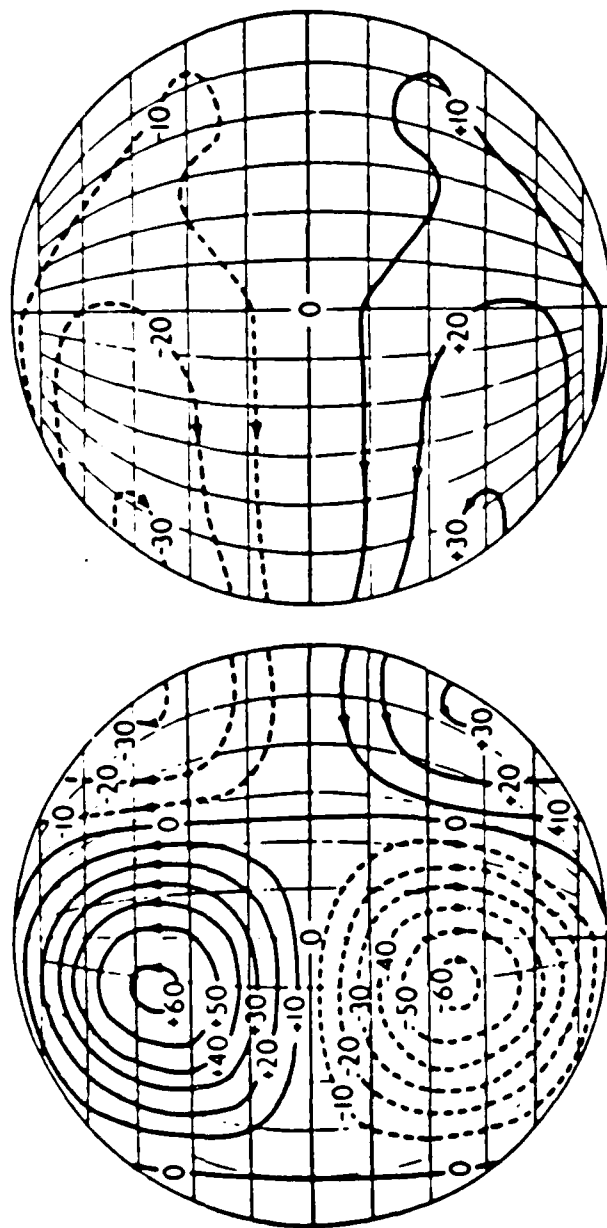Storm-time thermospheric winds can also drive electrical currents.

Figure 17. Sq current system. The overhead current system corresponding to sunspot minimum, equinoctal conditions. Numbers denote 10³A, so that the current flowing between any two neighboring streamlines is 10⁴A (after Chapman and Bartels, 1940; and Vestine, 1960) from Rishbeth and Garriot (1969).

Auroral heating due to geomagnetic storms sets up a large-scale "Hadley-cell" like circulation with winds flowing southward at mid-latitudes above 120 km (as described in Chapter IV). Conservation of angular momentum results in the development of a westward component in the wind. This westward wind sets up an induced electric field ($-\vec{V}$ X $\vec{B}$, $\vec{B}$ downward in the northern hemisphere) that yields an equatorward Pedersen current. This leads to the buildup of positive charges at the equator and negative charges at high latitudes, which results in a poleward polarization electric field just large enough to balance the equatorward current. The poleward electric field interacts with the earth's magnetic field ($\vec{B}$ down) leading to an eastward Hall current. When day/night conductivities are considered, the eastward Hall current is stopped at the terminator. Closure of the current leads to a current vortex similar to the Sq current system (on the same order of magnitude), but with the opposite sense. This is the anti-Sq current system (Blanc and Richmond, 1980). (Figure 18.)

The model generates both the northward electric field and the eastward current. Figure 19. shows the development of the electric field. Once the storm starts, the electric field starts growing and reaches a maximum of 4.52 mV/m, shortly after 12 hours. After storm shutoff, the electric field slowly starts to decrease in strength. The slow decrease results from the slow dissipation of the zonal winds, which continue to drive currents and electric fields even after the storm has stopped. (This was referred to by Lyons et al. (1985) as the neutral wind "flywheel".) Figure 20. shows the eastward Hall current. The current also builds up in strength as the storm progresses,

reaching a maximum of 56.5 mA/m after 12 hours (approx. 1.25×10^4 Amps, which is 1/5 the magnitude of the S_q current at 44° colatitude). Like the electric field, the current slowly decreases after the storm ends. In the next chapter, the model produced electric field will be compared to measurements.
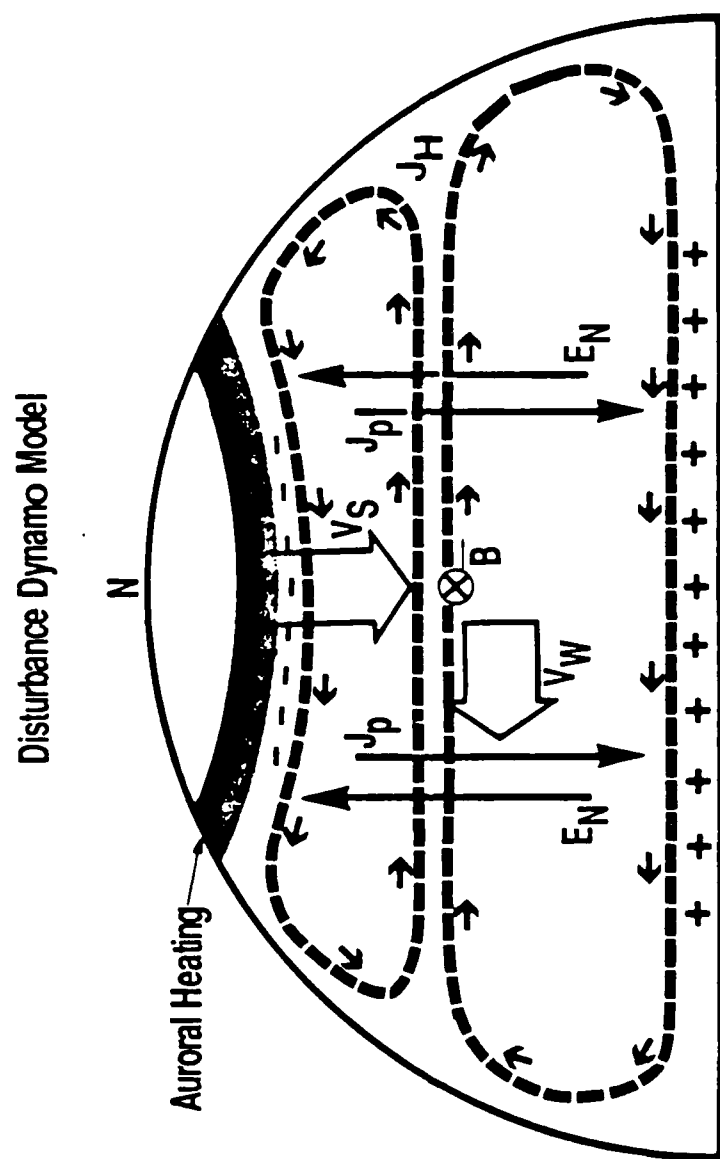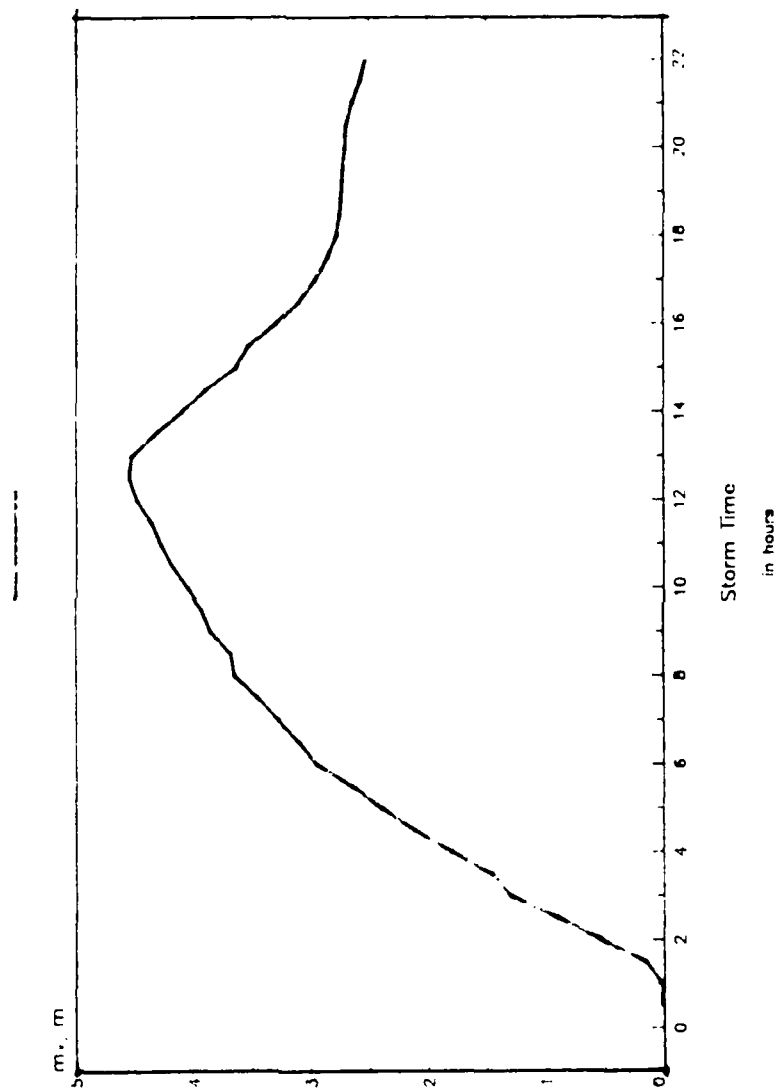
Disturbance Dynamo Model

Figure 18. The disturbance dynamo model.

Figure 19. Model generated northward electric field at 44° colatitude.
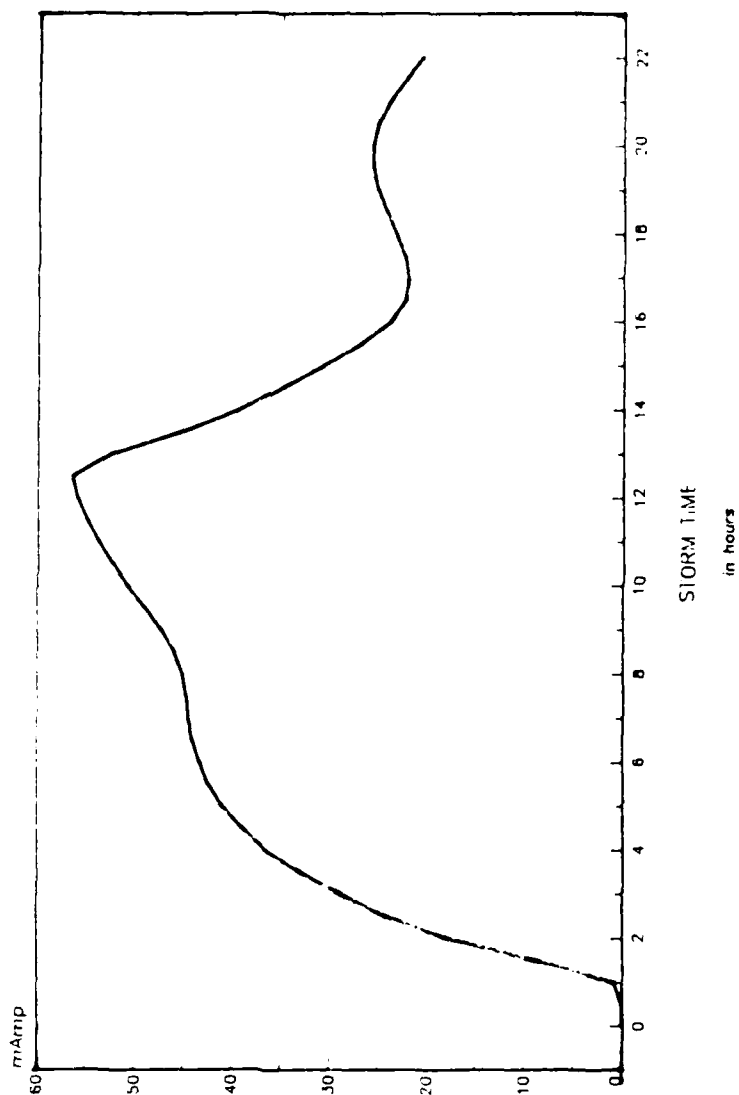
Figure 20. Model generated eastward electric current at 44° colatitude.

VI COMPARISON BETWEEN SAINT-SANTIN OBSERVATIONS AND MODEL

PREDICTIONS

In this chapter, neutral wind and electric field data from two storms analyzed by Mazaudier et al. (1985) will be compared to the model. (This section is from work done with C. Mazaudier and A.D. Richmond, Mazaudier et al.,1987.) The two storms are June 2, 1978, and April 19, 1977 (figures 21 and 23). The first storm shows good agreement between the observations and the simulations, while the second storm shows only fair agreement. The top panels in figures 21. and 23. show the AE index for these two storms. AE represents the time history of joule heating used in the simulations. The middle and bottom panels show the storm induced southward neutral winds derived from observations and the model produced winds. Note that the altitudes used in the first case differ from the second case. Figure 24. compares the observed electric field with model simulations for the April 19 case. (The electric field was unavailable for the June 1978 storm due to technical problems with the radar.)

The Saint Santin incoherent scatter radar was discussed in an earlier chapter. Not mentioned was the fact that the time resolution of the wind measurements is 30 minutes with an accuracy of $\pm$ 15 m/s. In addition, it is important to remember that the observed storm-induced winds are obtained by subtracting the quiet-time winds (Mazaudier et al., 1985) from the observations. The observed winds exhibit much day to day variablity even on magnetically quiet days. This variablity is not well understood and complicates the interpeta-

tion of storm-time variations.

Case #1 June 2, 1978

The middle panel of figure 21. shows a comparison between the neutral winds derived from observations and the neutral winds predicted by the model at 150 km. The observations show several peaks on the order of 70 to 80 m/s. The first peak from 9-10UT corresponds to the first peak in AE. The second peak in the neutral wind between 12 and 14UT corresponds to the second peak in the AE index. Then beginning at 17-18UT, there is a possibility of a third peak in the neutral winds before the observations terminate at dusk. The AE index shows a large increase from 14-20UT, but one can only speculate at what is happening to the neutral wind. This case shows a 3-4 hour time lag between increases in the AE index and increases in the neutral wind.

For this case, the computer model shows good qualitative agreement with the observations. The simulated winds show a southward wind component of about the same magnitude as the observations, although the time variations are different. The time lag between peaks in the model neutral winds and the AE index is about one hour shorter than the time lag between the observations and the AE index. The reason for this difference is not understood

Figure 22. shows a vertical profile of the meridional winds. On the lefthand side is the quiet-time average for June 1-14. On the righthand side is a comparison between the model wind profile and the observations averaged for June 2. Above 120 km, the model and the
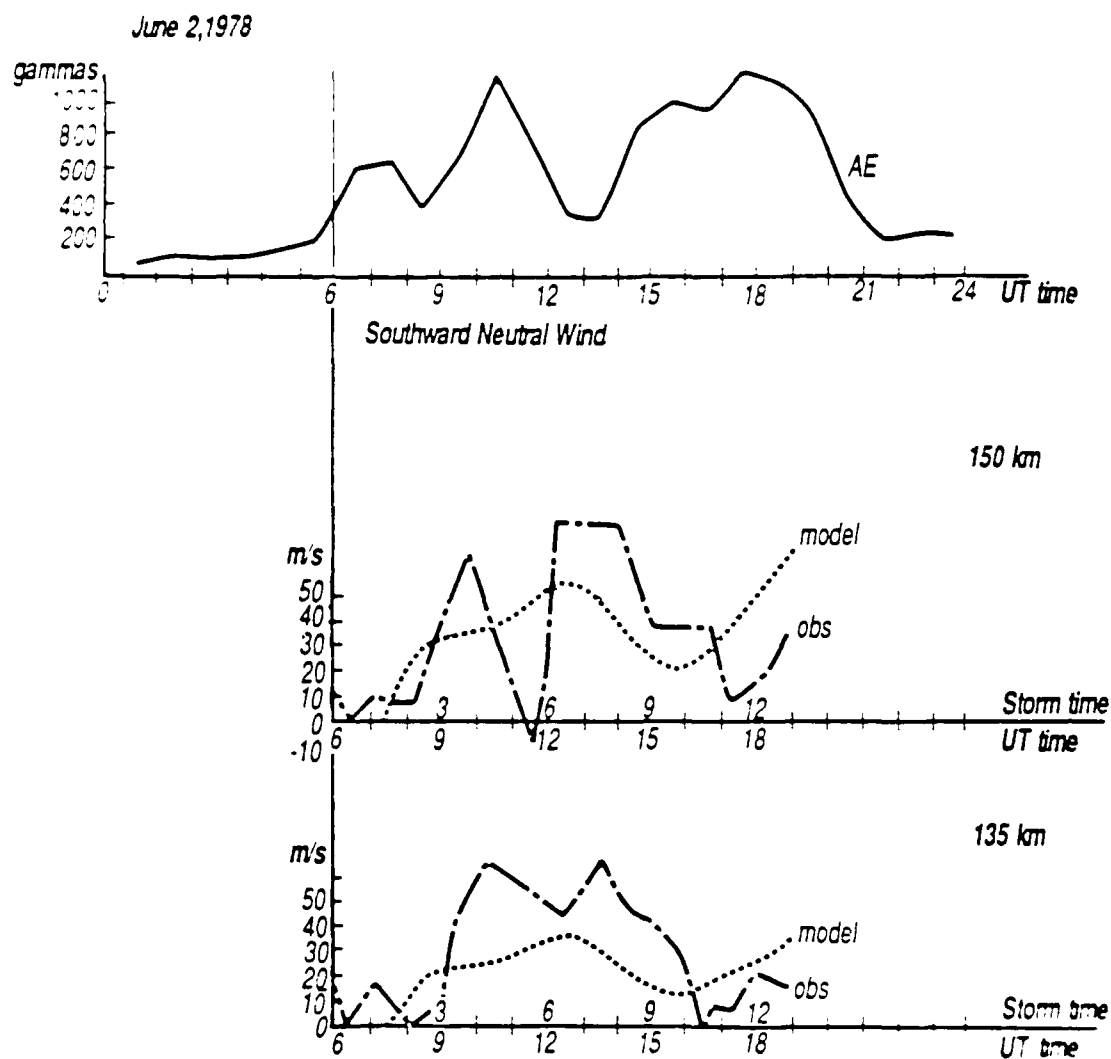
Figure 21. Disturbance on June 2, 1978. Top panel shows AE index for this case. Middle panel shows a comparison of observed southward neutral winds and model predictions over France at 150 Km. Bottom panel shows the same comparison, but at 135 Km.
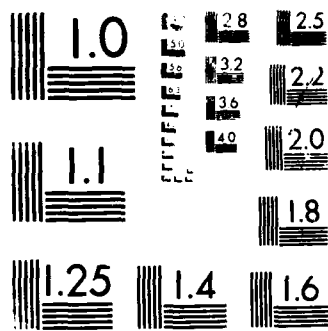
MICROCOPY RESOLUTION TEST CHART
NATIONAL BUREAU OF STANDARDS 1963-A
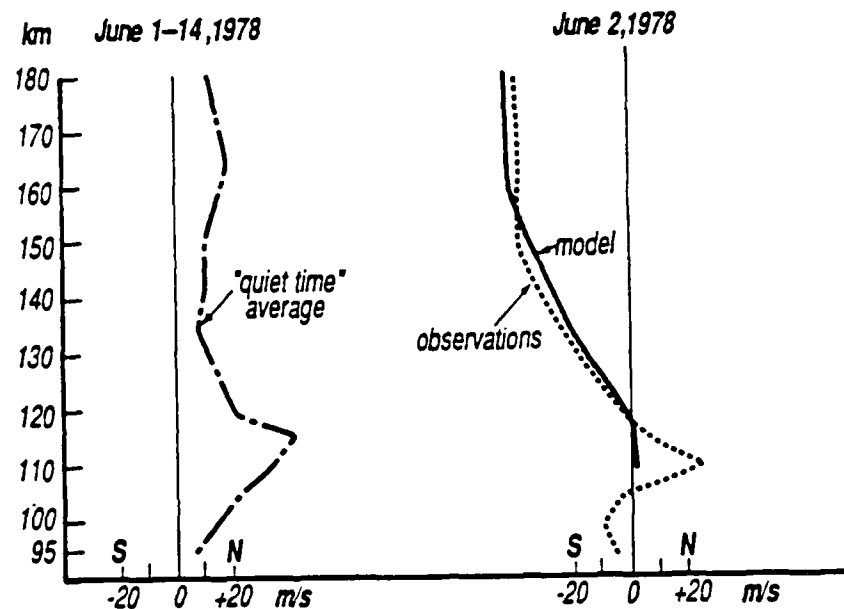
Figure 22. Vertical profiles of daily mean Saint Santin southward neutral winds. Lefthand side shows "quiet-time average" for June 1-14, 1978. Righthand side shows a comparison between the observations and the model for June 2, 1978.

observations show excellent agreement. Below 120 km, the model shows a slight northward flow, while the observations show a substantial northward flow down to 105 km. In the model, this northward flow represents the return mass flow, which balances the southward flow at higher altitudes. The observed wind is probably not perfectly symmetric in longitude, hence the average meridional mass flow is not required to balance out between different heights, as it must in the model. This allows for the observed winds at lower altitudes to differ from the model winds. Also, the observed winds below 120 km could be the result of the normal day to day variablity in the winds and not storm-related effects.

Case #2   April 19, 1977

The second case is the storm of April 19,1977. For this storm, the southward neutral wind disturbance, in figure 23., was already in progress above Saint-Santin when observations started. Hence, the exact time delay between the onset of auroral heating (vis-a-vis the AE index) and the onset of the neutral wind disturbance above Saint-Santin cannot be determined. The observed neutral winds are generally southward and show considerable structure. The model winds have the correct direction, but do not reproduce the observed structure. The model clearly overestimates the magnitude of the southward wind at 150 Km.

For this storm, measurements of the electric field are also available. The quiet-time electric field model of Blanc and Amayenc

(1979) was subtracted from the measurements. Figure 24. compares the observed northward electric field due to the disturbance with model predictions. It is important to note that the electric field observations are the result of two physical processes: the direct penetration of the magnetospheric convection electric field (Vasyliunas, 1970, 1972), and the ionospheric disturbance dynamo (Blanc and Richmond, 1980). The observations show a northward electric field on the order of 1-2 mV/m with much structure. This is comparable to the quiet-time amplitude measured by Blanc and Amayenc (1979). The amplitude and variablity is greatest from 06UT until 12UT when the auroral activity is strong and the penetration of the magnetospheric electric fields is probably most important. After 12UT when auroral activity has decreased the ionospheric dynamo should have its greatest relative importance on the electric field.

The model predicts the correct direction of the electric field but lacks the structure shown in the observations and overpredicts the magnitude. This overprediction is likely related to the overprediction of wind strengths at 150 km, seen in figure 23. The generation of the electric fields by the disturbance dynamo occurs predominately below 150 km, where daytime conductivities are greatest, and the model may be significantly overestimating these E region winds. Causes of this differences may be linked to the inherent limitations of the two-dimensional model and to possible deviations of the joule heating from the assumed parameterization based on the AE index.
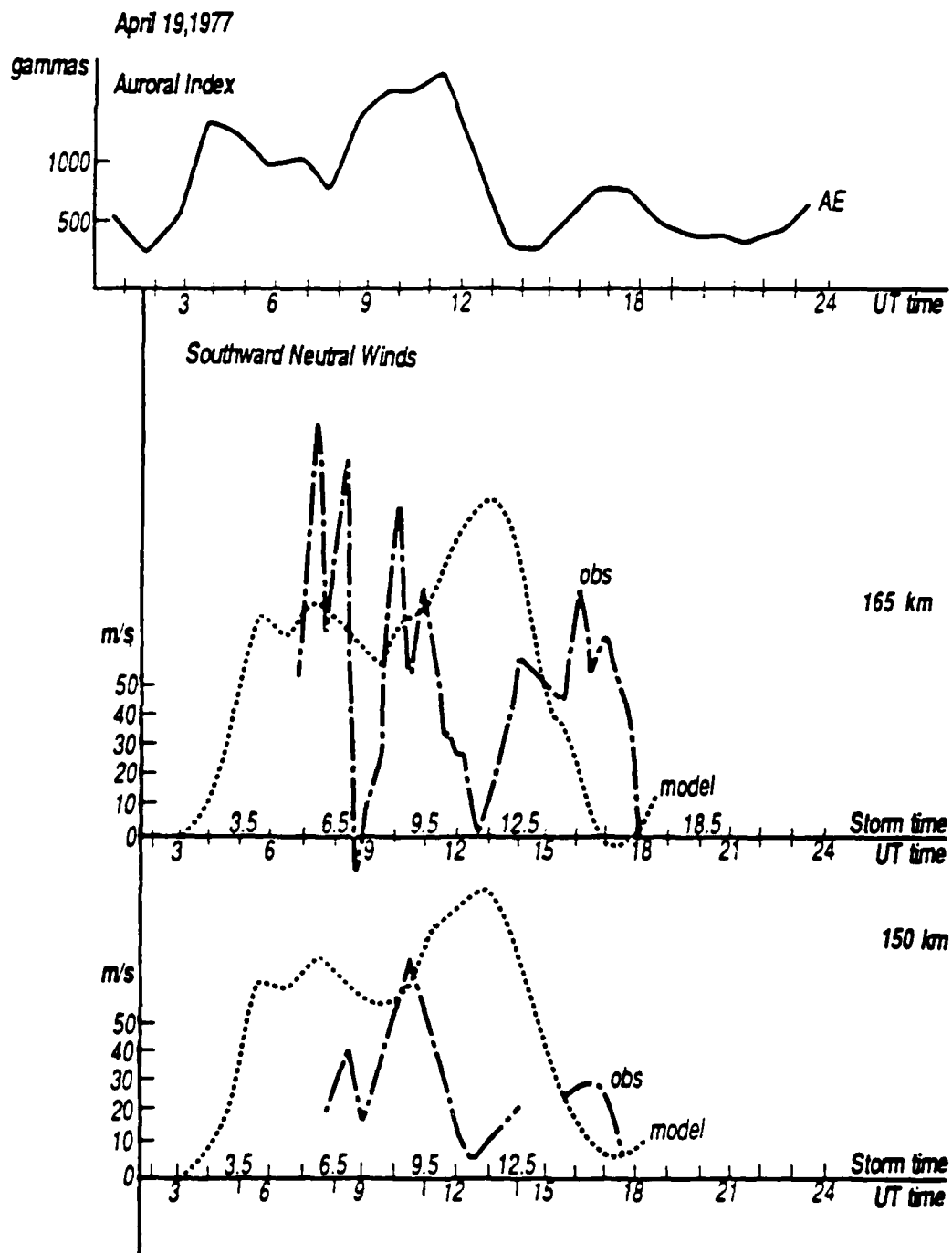
Figure 23. Disturbance on April 19,1977. Same as Figure 21 except for April 19. Middle panel is at 165 Km, and bottom panel is at 150 Km.
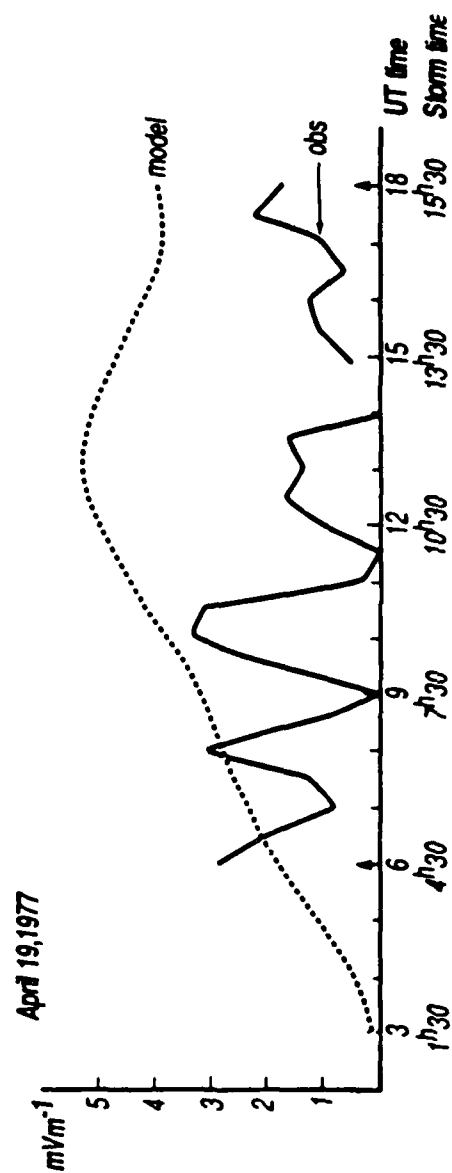
Figure 24. Comparison between observed northward electric field and the model predicted electric field over Saint Santin on April 19, 1977.

VII   CONCLUSIONS & FUTURE WORK

The results of Richmond and Matsushita (1975) showed that thermospheric circulation due to the impulsive heating associated with a geomagnetic storm is initially characterized by a period of transient gravity waves. The computer simulations presented here confirm that work, which is not surprising since I used essentially the same model. Also, these computer simulations show the development of a mean circulation associated with storm-time heat inputs. This is in agreement with the observations of Mazaudier et al. (1985) and the modelling work of Blanc and Richmond (1980). Also in agreement with Blanc and Richmond, the results here show that the storm-time motions of the thermosphere drive an electrical current system that is opposite in direction to, and on the same order of magnitude as the quiet-time Sq current system. The current generated by the generic storm was approx. 1/5 the magnitude of the S_q current at 44° colatitude.

Both, the mean circulation and the waves, transport heat from high to low latitudes. Heat transport by the mean circulation accounts for 2/3 of the low latitude temperature increase. This again confirms the work of Richmond and Matsushita (1975). Richmond (1979b) showed that low latitude heating due to heat transport via the mean circulation dominated over heating due to the viscous dissipation of gravity waves. Not considered in that work, however, was heating due to heat transport by the waves themselves. This mechanism could be important, especially during the first few hours of a geomagnetic storm.   It remains as a topic for future work.

Additionally, work done with C. Mazaudier and A.D. Richmond (Mazaudier et al., 1987) and presented here (chapter IV) showed that the two-dimensional model sucessfully reproduced the large-scale storm-time hydrodynamical and electrodynamical features of the thermosphere in one case. In another case, the model was less sucecessful in re-producing these features. The details of these features also need to be worked out.

Richmond and coworkers are aware of the limitations of the model and are working to improve it. I hope to participate in this work. Possible improvements to the model include adding tidal effects to the bottom of the model, and using a better parameterization for the auroral heating as the current parameterization is only accurate by a factor of two.

The latitudinal variations could be better understood by comparing the wind observations from two incoherent scatter radars at different latitudes (Millstone Hill and Arecibo) with model outputs. Longitu-dinal variations that are normally absent from 2d simulations also need to be addressed. This can be done ideally by using a 3d model like the NCAR TGCM, or by incorporating some sort of longitudinal variation into the current 2d model.

APPENDIX 1

List of Symbols:

a	radius of earth.
$\vec{B}$	geomagnetic field.
B_r	radial component of $\vec{B}$.
$\hat{b}$	unit vector in the direction of $\vec{B}$.
C_p	specific heat of air per unit mass.
$\vec{E}$	electrostatic field.
e	magnitude of electronic charge.
F	arbitrary operator.
g	acceleration of gravity, 9.5 m/s^2.
H	atmospheric scale height.
ΔH	variation of the H component of $\vec{B}$.
h	altitude.
I	inclination of geomagnetic field below horizontal.
m_e, m_i	mass of electron and ion (mean).
P	pressure.
P_0	pressure at 80 km, 1.038 Pa.
Q_0	background heat source per unit mass and time.
q	upward heat flux.
R	gas constant for air.
r	ratio of ion collision to gyrofrequencies.
T	temperature.
t	time.
U_j	hemispheric Joule heating rate.

$\vec{V}$ horizontal air velocity.

Z dimensionless height coordinate.

γ $= C_p/(C_p-R)$.

ϵ specific enthalpy plus kinetic energy density per unit mass of air.

θ colatitude.

κ_m molecular coefficient of heat conduction.

κ_t turbulent coefficient of heat conduction.

μ_m molecular coeffiecient of viscosity.

μ_t turbulent coeffiecient of viscosity.

ν ion-neutral collision frequency.

ρ air density.

σ_1,σ_2 Pedersen and Hall conductivities.

σ_p height intergrated Pedersen conductivity.

τ horizontal viscous stress.

ϕ east longitude.

Ψ arbitrary function of time.

ω angular rotation rate of the earth, $7.29 \times^{-5}\ s^{-1}$.

REFERENCES

Ahn, B., S.I. Akasofu, and Y. Kamide, 1983, The Joule heat production rate and the particle injection rate as a function of the geomagnetic indices AE and AL, J. Geophys Res., 88, A8, 6275-6287.

Banks, P., 1977, Observations of Joule and particle heating in the auroral zone, J. Atmos. Terr. Phys.,39, 179-193.

Banks, P., J.C. Feder, and J.R. Doupnik, 1981, Chatanika radar observations relating to the latitudinal and local time variation of Joule heating, J. Geophys. Res., 87, A8, 6869-6878.

Baumjohann, W., and Y. Kamide, 1984, Hemispherical Joule heating and the AE indices, J. Geophys. Res., 89, A1, 383-388.

Blanc, M., and P. Amayenc, 1979, Seasonal variations of the ionospheric ExB drifts above Saint Santin on quiet days, J. Geophys. Res., 84, A6, 2691-2704.

Blanc, M., A.D. Richmond, 1980, The ionospheric disturbance dynamo, J. Geophys. Res., 85, 1669-1686.

Brekke, A., 1976, Electric fields, Joule and particle heating in the high latitude thermosphere, J. Atmos. Terr. Phys., 38, 887-895.

Brekke, A., and C.L. Rino, 1978, High-resolution altitude profiles of the auroral zone energy dissipation due to ionospheric currents, J. Geophys. Res., 83, 2517-2524.

Burnside, R.G., F.A. Herrero, J.W. Meriwether Jr., and J.G. Walker, 1981, Optical observations of thermospheric dynamics at Arecibo, J. Geophys. Res., 86, A7, 5532-5540.

Burnside, R.G., R.A. Behnke, and J.G. Walker, 1983, Meridional neutral winds in the thermosphere at Arecibo: Simultaneous incoherent and airglow observations, J. Geophys. Res., 88, A4, 3181-3189.

Chapman, S., 1931, The absorption and dissociative or ionizing effect of monochromatic radiation in an atmosphere on a rotating earth, Proc. Phys. Soc. (London), 43, 26-45.

Chapman, S., and J. Bartels, 1940, Geomagnetism, Oxford Univ. Press (Clarendon), London.

Chimonas, G., and C.O. Hines, 1970, Atmospheric gravity waves launched by auroral currents, _Planet. Space Sci._, 18, 565-582.

Dickinson, R.E., and J.E. Geisler, 1968, Vertical motion field in the middle thermosphere from satellite drag densities, _Mon. Weather Rev._, 96, 606-616.

Dickinson, R.E., E.C. Ridley, and R.G. Roble, 1975, Meridional circulation in the thermosphere, I. Equinox conditions, _J. Geophys. Res._, 32, 1737-1754.

Duboin, A.L., and Y. Kamide, 1984, Latitudinal variations of Joule heating due to auroral electrojets, _J. Geophys. Res._,89, 245-251.

Francis, S.H., 1975, Global propagation of atmospheric gravity waves: A review, _J. Atmos. Terr. Phys._, 37, 1011-1054.

Hanson, W.B., and H.C. Carlson, 1977, The ionosphere, _The Upper Atmosphere and Magnetosphere_, National Academy of Sciences, Washington D.C., 84-101.

Hargreaves, J.K., 1979, _The Upper Atmosphere and Solar-Terrestrial Relations_, Van Nostrand and Reinhold Company, London.

Harper, R.M., 1973, Nighttime meridional neutral winds near 350 Km at low to mid-latitudes, _J. Atmos. Terr. Phys._, 35, 2023-2034.

Hays, P.B., and R.G. Roble, 1971, Direct observations of thermospheric winds during geomagnetic storms, _J. Geophys. Res._, 76, 5316-5321.

Hays, P.B., J.W. Meriwether, and R.G. Roble, 1979, Nighttime thermospheric winds at high latitudes, _J. Geophys. Res._, 84, 1905-1913.

Hedin, A.E., J.E. Salah, J.V. Evans, C.A. Reber, G.P. Newton, N.W. Spencer, D.C. Kayser, D. Alcayade, P.Bauer, L.L. Cogger, and J.P. McClure, 1977, A global thermospheric model based on mass spectrometer and incoherent scatter data: MSIS1, N_2 density and temperature, _J. Geophys. Res._, 82, 2139-2147.

Hedin, A.E., 1983, A revised thermospheric model based on mass spectrometer and incoherent scatter data: MSIS-83, _J. Geophys. Res._, 88, 10170-10188.

Hernandez, G., and R.G. Roble, 1976a, Direct measurements of nighttime thermospheric winds and temperatures 1. Seasonal variations during geomagnetic quiet periods, _J. Geophys. Res._, 81, 2065-2074.

Hernandez, G., and R.G. Roble, 1976b, Direct measurements of nighttime thermospheric winds and temperatures 2. Geomagnetic storms, J. Geophys. Res., 81, 5173-5181.

Hernandez, G., and R.G. Roble, 1977, Direct measurements of nighttime thermospheric winds and temperatures 3. Monthly variation during solar minimum, J. Geophys. Res., 82, 5505-5511.

Hernadez, G., and R.G. Roble, 1978, Observations of large-scale thermospheric waves during geomagnetic storms, J. Geophys. Res., 83, A12 5531-5538.

Hernandez, G., and R.G. Roble, 1984, The geomagnetic quiet nighttime thermospheric wind pattern over Fritz Peak Observatory during solar cycle minimum and maximum, J. Geophys. Res., 89, A1, 327-337.

Hines, C.O., 1960, Internal atmospheric gravity waves at ionospheric heights, Can. J. Phys., 38, 1441-1481.

Hines, C.O., 1974, Propagation velocities and speeds in ionospheric waves: A review, J. Atmos. Terr. Phys., 36, 1179-1204.

Jacchia, L.G., 1965, Static diffusion models of the upper atmosphere with empirical temperature profiles, Smithsonian Contrib. Astro-Phys., 8.

Jacchia, L.G., 1971, Revised static models of the thermosphere and exosphere with empirical temperature profiles, Spec. Rep. 332, Smithson. Astrophys. Observ., Cambridge, Mass.

Kamide, Y., A.D. Richmond, and S. Matsushita, 1981, Estimation of ionospheric electric fields, ionospheric currents, and field aligned currents from ground magnetic records, J. Geophys.Res., 86, 801-813.

Kamide, Y., and A.D. Richmond, 1982, Ionospheric conductivity dependence of electric fields and currents estimated from ground magnetic observations, J. Geophys. Res., 87, 8331-8337.

Kamide, Y., and S.I. Akasofu, B.H. Ahn, W Baumjohann, and J. Kisabeth, 1982, Total current of the auroral electrojet estimated from IMS Alaska meridian chain of magnetic observatories, Planet. Space Sci., 30, 621-625.

Killeen, T.L., R.G. Roble, R.W. Smith, N.W. Spencer, J.W. Meriwether, Jr., D. Rees, G. Hernandez, P.B. Hays, L.L. Cogger, D.P. Sipler, M.A. Biondi, and C.A. Tepley, 1986, Mean neutral circulation in the winter polar F region, J. Geophys. Res., 91, A2, 1633-1649.

Killeen, T.L., 1987, Energetics and dynamics of the earth's thermo-
sphere, Reviews of Geophysics, 25, 3, 433-454.

Lyons, L.R., 1980, Generation of large-scale regions of auroral cur-
rents, electric potential, and precipitation by the divergence of
the convection electric field, J. Geophys. Res., 85, A1, 17-24.

Lyons, L.R., T.L. Killeen, and R.L. Waltersheid, 1985, The neutral
wind "flywheel" as a source of quiet-time , polar-cap currents,
Geophys. Res. Lett., 12, 2, 101-104.

Mazaudier, C., R. Bernard, S.V. Venkateswaran, 1985, Saint Santin
radar observations of lower thermospheric storms, J. Geophys. Res.,
90, 3, 2885-2895, correction J. Geophys. Res., 90, 7, 6685-6686.

Mazaudier, C., A.D. Richmond, and D. Brinkman, 1987, On thermospheric
winds produced by auroral heating during magnetic storms and
associated electric fields, Annales Geophysicae, submitted.

Richmond, A.D. and S. Matsushita, 1975, Thermospheric response to a
magnetic substorm, J. Geophys. Res., 80, 9, 2839-2850.

Richmond, A.D., 1979a, Ionospheric wind dynamo theory: A review, J.
Geomag. Geoelectr., 31, 287-310.

Richmond, A.D., 1979b, Thermospheric heating in a magnetic storm:
Dynamic transport of energy from high to low latitudes, J. Geo-
phys. Res., 84, A9, 5259-5266.

Richmond, A.D., 1983, Thermospheric dynamics and electrodynamics,
Solar-Terrestrial Physics, B.L. Carovillano and J.M. Forbes
(eds.), 523-607.

Rishbeth, H., and O.K. Garriott, 1969, Introduction to Ionospheric
Physics, Academic Press, New York.

Rishbeth, H., 1972, Thermospheric wind and the F region: A review,
J. Atmos. Terr. Phys., 34, 1-47.

Roble, R.G., B.A. Emery, J.E. Salah, and P.B. Hays, 1974, Diurnal
variation of the neutral thermospheric wind determined from in-
coherent scatter radar data, J. Geophys. Res., 79, 2868-2876.

Roble, R.G., 1977, The thermosphere, The Upper Atmosphere and Magneto-
sphere, National Academy of Science, Washington D.C., 57-71.

Roble, R.G., A.D. Richmond, W.L. Oliver, and R.M. Harper, 1978, Iono-
spheric effects of a gravity wave launched by the September 18,
1974, sudden commencement, J. Geophys. Res., 83, A3, 999-1009.

Salah, J.E., and J.M. Holt, 1974, Midlatitude thermospheric winds from

incoherent scatter radar and theory, Radio Sci., 9, 301-313.

Sipler, D.P., and M.A. Biondi, 1979, Midlatitude F region neutral
    winds and temperatures during the geomagnetic storm of March
    26, 1976, J. Geophys. Res., 84, 37-40.

Sipler, D.P., M.A. Biondi, and R.G. Roble, 1981, Midlatitude F-region
    neutral winds and temperatures during the priority regular world
    day 14 Aug. 1980, Planet. Space Sci., 29, 12, 1367-1372.

Sipler, D.P., B.B. Luokkala, and M.A. Biondi, 1982, Fabry-Perot deter-
    minations of mid-latitude F-region neutral winds and temperatures
    from 1975 to 1979, Planet. Space Sci., 20, 1025-1032.

Vasyliunas, V.M., 1970, Mathematical models of magnetospheric convec-
    tion, in Particles and Fields in the Magnetosphere, edited by B.M.
    McCormac, D. Reidel, Hingham, Mass., 60-70.

Vasyliunas, V.M., 1972, The interrelationship of the magnetospheric
    processes, in Earth's Magnetospheric Processes, edited by B.M.
    McCormac, D, Reidel, Hingham, Mass., 29-40.

Vestine, E.H., 1960, The upper atmosphere and geomagnetism, in Physics
    of the Upper Atmosphere, J.A. Ratcliffe, ed., Chapter 10, Academic
    Press, New York.

Vickrey, J.F., R.R. Vondrak, and S.J. Matthews, 1982, Energy deposit-
    ion by precipitating particles and Joule dissipation in the auro-
    ral ionosphere, J. Geophys. Res., 87, 5184-5176.

Waltersheid, R.L., and D.J. Boucher, 1984, A simple model of the tran-
    sient response of the thermosphere to impulsive forcing, J. Atmos.
    Sci., 41, 1062-1072.

END
DATE
FILMED
JAN
1988